



## PAPER

# Differences in cortical contractile properties between healthy epithelial and cancerous mesenchymal breast cells








## OPEN ACCESS

RECEIVED  
4 March 2020REVISED  
23 August 2021ACCEPTED FOR PUBLICATION  
9 September 2021PUBLISHED  
18 October 2021

Original content from  
this work may be used  
under the terms of the  
[Creative Commons  
Attribution 4.0 licence](#).

Any further distribution  
of this work must  
maintain attribution to  
the author(s) and the  
title of the work, journal  
citation and DOI.



Enrico Warmt<sup>1</sup> , Steffen Gresser<sup>1</sup> , Eliane Blauth<sup>1</sup>, Xiaofan Xie<sup>1</sup> ,  
Hans Kubitschke<sup>1</sup> , Roland Stange<sup>1</sup>, Frank Sauer<sup>1</sup> , Jörg Schnauß<sup>1,2,3</sup> ,  
Janina M Tomm<sup>4</sup>, Martin von Bergen<sup>4</sup> and Josef A Käs<sup>1,\*</sup> 

<sup>1</sup> Peter Debye Institute for Soft Matter Physics, Leipzig University, Linnéstraße 5, 04103 Leipzig, Germany

<sup>2</sup> Fraunhofer Institute for Cell Therapy and Immunology, Perlickstraße 1, 04103 Leipzig, Germany

<sup>3</sup> Unconventional Computing Laboratory, Department of Computer Science, University of the West of England, Bristol, United Kingdom

<sup>4</sup> Department of Molecular Systems Biology, Helmholtz Centre for Environmental Research—UFZ, Permoserstr. 15, 04318 Leipzig, Germany

\* Author to whom any correspondence should be addressed.

E-mail: [jkaes@physik.uni-leipzig.de](mailto:jkaes@physik.uni-leipzig.de)

**Keywords:** biophysics, tissue formation, cell contractility, multicellular spheroids, blebbistatin, actin cortex, actin stress fibers

Supplementary material for this article is available [online](#)

## Abstract

Cell contractility is mainly imagined as a force dipole-like interaction based on actin stress fibers that pull on cellular adhesion sites. Here, we present a different type of contractility based on isotropic contractions within the actomyosin cortex. Measuring mechanosensitive cortical contractility of suspended cells among various cell lines allowed us to exclude effects caused by stress fibers. We found that epithelial cells display a higher cortical tension than mesenchymal cells, directly contrasting to stress fiber-mediated contractility. These two types of contractility can even be used to distinguish epithelial from mesenchymal cells. These findings from a single cell level correlate to the rearrangement effects of actomyosin cortices within cells assembled in multicellular aggregates. Epithelial cells form a collective contractile actin cortex surrounding multicellular aggregates and further generate a high surface tension reminiscent of tissue boundaries. Hence, we suggest this intercellular structure as to be crucial for epithelial tissue integrity. In contrast, mesenchymal cells do not form collective actomyosin cortices reducing multicellular cohesion and enabling cell escape from the aggregates.

## 1. Introduction

Biomechanical properties of eukaryotic cells are governed by passive and active cytoskeletal structures [1, 2]. Their interplay is not only crucial for cell integrity but also for tissue stability. However, although these structures have been in the focus of many studies, it remains challenging to simultaneously address passive and active and single and multicellular properties simultaneously [3–5]. Generally, active cellular properties have recently gained increasing attention due to their eminent impact on single-cell and tissue functions [3, 4, 6–10, 11, 12]. An effect arising from the interplay of active and passive components is cellular contractility, which explains cell motility and invasion and is also an integral part of tissue formation models [10, 21]. For instance, cancer and mesenchymal cells display higher contractility when migrating through the extracellular matrix (ECM) in comparison to healthy epithelial cells [21–36].

For cell mechanics and particularly for contractility, actomyosin interactions play the dominant role [37–39]. However, different actin structures can cause different types of contractile behavior. On the one hand, aligned stress fibers cause a dipole-like contractility [22, 40–45], at the same time, disordered cortical actomyosin networks cause isotropic contractions [10, 16, 46]. Both structures are built of passive cross-linked actin filaments and force-generating myosin II motor proteins [1, 47–49]. Stress fibers are actin

bundles that span between focal adhesion complexes, which anchor cells to their extracellular environment [1]. Their main function lies in propulsion during migration [21]. The actomyosin cortex is a thin, disordered, shell-like structure underlying the plasma membrane [16, 44, 46, 50]. It creates a cortical tension, which is regulated by intra- or extracellular signals and influences cell shape formation, -polarization, -migration as well as tissue morphogenesis [10, 16, 46, 50–52]. The role of cortical tension is well-documented during cell division; however, adequate quantification is still challenging [10, 50, 52–54]. Both contractile modes can contribute simultaneously to cell mechanics. However, current experimental approaches maintain difficulties in decoupling them [3, 16]. Moreover, contractility plays a fundamental role in a vast amount of cell- and tissue functions, while a clear and consistent use of the term ‘contractility’ is missing.

Here, we used a tailored set of methods to elucidate the diverse roles of active contractility in specific cell and tissue functions. First, we examined the cortical contractile behavior of *suspended* cells, which lack actin stress fibers [16, 46]. We use the optical stretcher (OS) to circumvent these limitations and to quantify cortical properties (active *and* passive) of whole suspended cells in a contact-free manner and with high throughput. We observed that epithelial single cells expressed higher cortical contractility compared to mesenchymal cells. Further, we correlated these single-cell properties to multicellular assembly and showed that collective cortical contractility stabilizes cell–cell adhesion, which seems crucial in epithelial tissue stability. In contrast, mesenchymal cells lack collective cortical contractility, which seems essential for single-cell escape into the ECM.

Our results provide experimental evidence that supports recent theories of tissue boundary formation during development. In fact, expansions of the standard differential adhesion hypothesis (eDAH) [55], have been proposed based on active cortical tension that can—additionally to cell–cell adhesion—stabilize cell boundaries and keep cell clusters together via a collective actin cortex [56]. Our results have important implications for cell jamming, segregation, collective motion, and single-cell escape.

We introduce the notion of cortical vs stress-fiber contractility, which we propose as a new key concept to understand the sheer variety of cellular function across entirely different environments, from single cells and cell clusters to invasion. Altogether, we suggest a new classification where healthy epithelial cells express a higher cortical contractility, and in contrast, mesenchymal cells favor stress-fiber-based contractility.

## 2. Results

### 2.1. Cortical contractility of single suspended cells

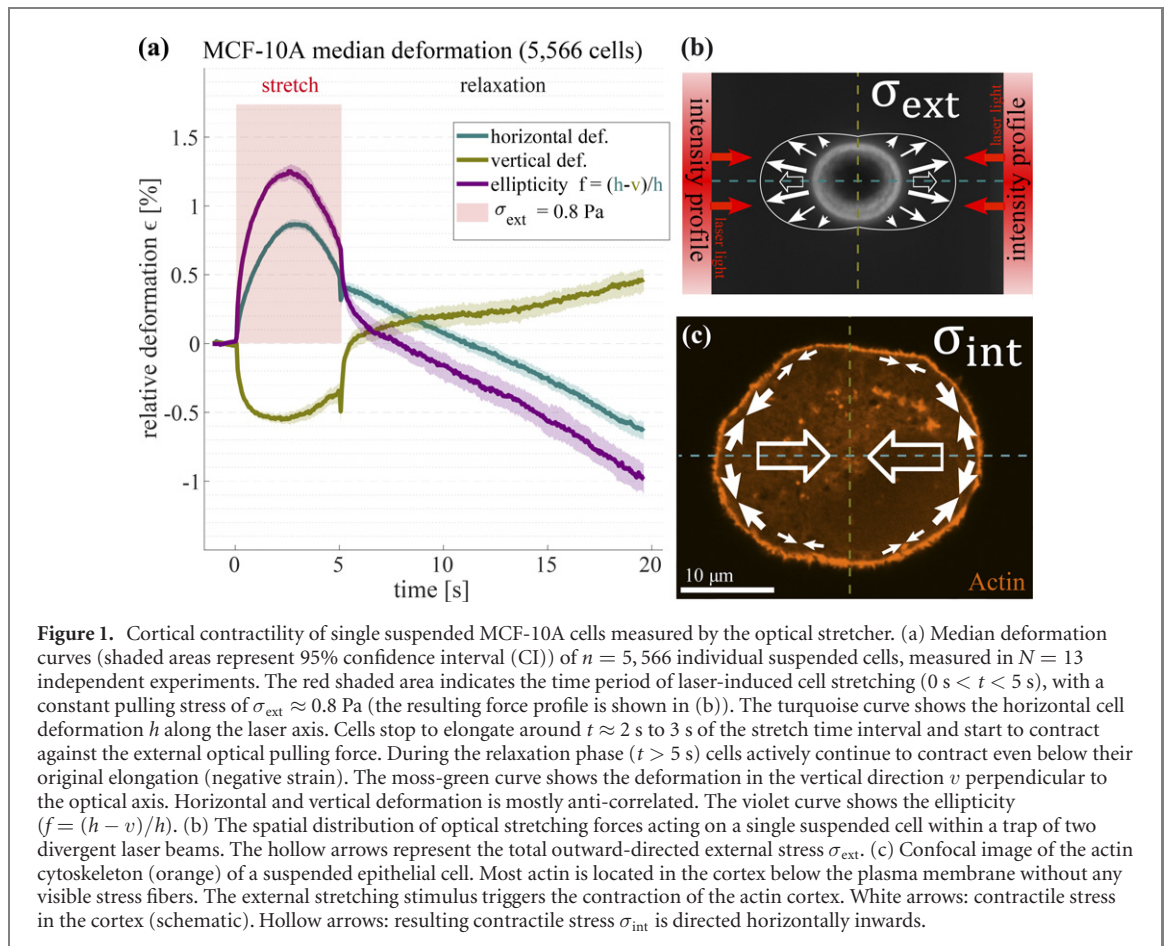
Up to now, there is no appropriate contact-free technique to quantify cortical contractility of fully suspended cells [10, 16]. Here, we use the OS to measure this quantity in cells, excluding any effects caused by contacts or substrate adhesion, such as focal adhesion points and stress fiber formation. The OS has so far been used to investigate particularly passive biomechanical changes such as cell stiffness [37, 57–59].

#### 2.1.1. Suspended cells contract actively against external stretching force

The OS optically traps and stretches cells in an automated way, measuring the creep deformation as a response to the step-stress stretch force (technical details can be found in materials and methods). The two laser beams exert a stretching (pulling) stress  $\sigma_{\text{ext}}$  on the trapped cells [57, 60, 61] (figure 1). During the stretch, cells initially elongate with a slowly increasing strain  $\epsilon$  as in a passive creep deformation.

However, for some cell types, the strain starts to decrease during the step stress (figure 1 and supporting video). As the suspended cells have no contact with the walls, the decreasing strain against a constant external stress can only be explained by an active contraction of the cells. This effect was not reported in most OS studies so far (an exception being [62, 63]) because cells were typically stressed for only 2 s [37, 59, 64, 65]. However, the contractile effect became evident only during longer stretches, such as the 5 s interval we used in this study (figure 1(a)). After a few seconds, the optical forces (figure 1(b) and [38, 59, 61, 66, 67]) induced a mechanosensitive cell reaction, which can be monitored as a deformation of the long axis of the cell or even more obvious via the elliptic shape ( $\epsilon = (h - v)/h$ ). Here,  $h$  and  $v$  were the cell’s horizontal and vertical relative deformations of the cell along the optical force axis and perpendicular to it (figure 1(a)). In a measurement of  $n = 5,566$  epithelial MCF-10A cells, the relative ellipticity  $\epsilon$  increased by  $1.2 \pm 0.1\%$  within the initial two to 3 s. Subsequently,  $\epsilon$  decreased although the external force was still acting on the cell. This led to a rounding up of the cell shape during the later phase of the optical force application.

We quantified the internal contractile stress by fitting an adapted standard linear solid model (SLS) with an additional linear contractile term to the experimental data (see materials and methods section and figure 11). This model enabled us to assess the contributions of both passive and active cell properties. It extracts cell elasticity  $E$ , viscosity  $\eta$ , cortical pretension (or stiffness)  $E2$ , and an additional active cortical



contractile stress  $\sigma_{\text{int}}$ . We found that cells built up an increasing internal contractile stress that was similar in magnitude to the external stress applied by the OS (on the order of 1 Pa). There were, however, significant differences in contractility between different cell lines, which is demonstrated in the next section.

Moreover, we found that the MCF-10A cells continued contracting during the relaxation phase after stress release. The median ellipticity reached an average of  $-1.0 \pm 0.1\%$ , i.e. cells mostly ended up rounder than before the stretching procedure. Thus, the active contraction is triggered by an external stress and continues after it has vanished, emphasizing the active nature of this process (figure 1(a)).

Further, we found that the contractility  $\sigma_{\text{int}}$  depends on the applied stress  $\sigma_{\text{ext}}$ , which suggests that the contractility is a mechanosensitive effect. Increased external stress ( $\sigma_{\text{ext}}$ ) in average induced stronger contractile responses (figures 13 and 14 (<https://stacks.iop.org/NJP/23/103020/mmedia>)). In addition, individual cells that deformed with higher strain ( $\epsilon$ ) responded with stronger opposing contractile forces, particularly after stress release (figure 19(b)).

One measurement-specific artifact we would like to mention is that cells are inevitably heated during the stretching procedure since the OS uses laser light. However, we could partially decouple heating effects from mechanical effects by employing additional heating lasers to regulate the temperature in the vicinity of the cell (see materials and methods section and [66, 68–71]). We found that cells that experience less stretch force were less contractile at given temperatures, which again suggests that contractility is primarily force-dependent (figures 13 and 14). By controlling the temperature of the environment around the cells, we found that cell contractility also depends on temperature (figure 15). In our experiments, the active contractility was strongest at physiological temperatures of about  $T_{\text{eff}} = 37^\circ\text{C}$ , which we used throughout this study unless stated otherwise. At elevated temperatures beyond physiological conditions  $T_{\text{eff}} > 40^\circ\text{C}$ , cortical contractile behavior disappeared (figure 15).

### 2.1.2. Cortical contractility is driven by actomyosin

The actin in *suspended* cells is mostly found in the cortex (figure 1(c)) [10, 16, 37, 46, 52], and can exert contractile forces [10, 50, 52, 53]. To check whether the contractility we observed in the OS is driven by actomyosin activity in the cortex, we inhibited myosin by treating the cells with  $5 \mu\text{M}$  blebbistatin (B).

We found that the blebbistatin-treated MCF-10A cells did not show an obvious active contractile response anymore and displayed significantly higher maximal deformations. Quantitatively, the contractility

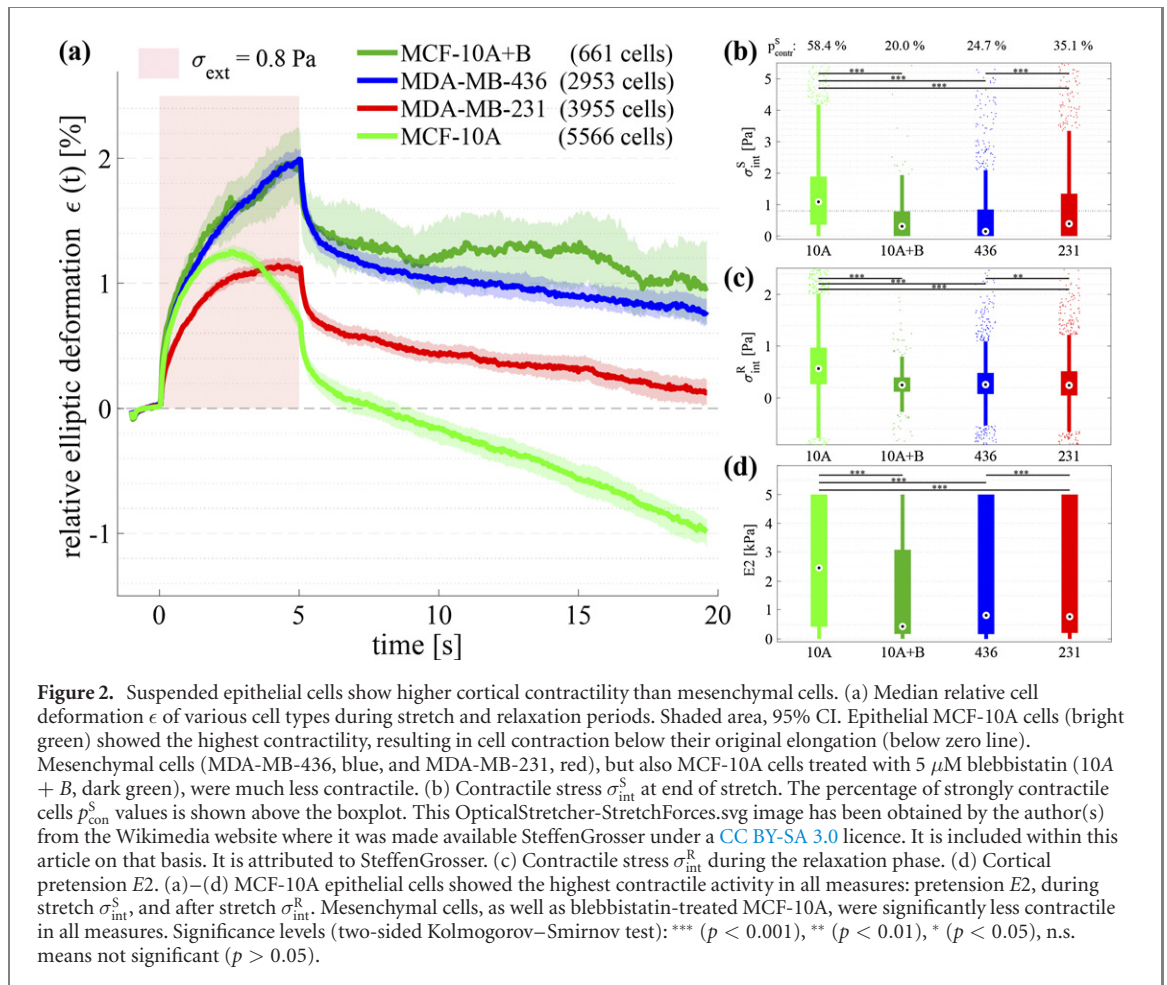


**Table 1.** Cortical contractile parameters of single suspended cells measured in the OS. Values listed are medians and quantiles in parenthesis.  $\Delta\sigma_{\text{int}}^{\text{S}}$  represents the increasing rate of internal contractile stress against optical stress ( $\sigma_{\text{ext}} = 0.8 \text{ Pa}$ ).  $\sigma_{\text{int}}^{\text{S}}$  denotes the cumulative internal contractile stress at the end of laser-induced stretching ( $\sigma_{\text{int}}^{\text{S}} = \Delta\sigma_{\text{int}}^{\text{S}} * 5 \text{ s}$ ).  $\sigma_{\text{int}}^{\text{R}}$  describes the continuing contractile stress during relaxation.  $\gamma_{\text{CST}}^{\text{R}}$  approximates CST, which was calculated by  $\gamma_{\text{CST}}^{\text{R}} = F \frac{d\epsilon}{dA}$ , where  $F$  is cells internal contractile force,  $d\epsilon$  is the change of absolute elongation and  $dA$  accounts for the change in cells absolute surface area (all during relaxation). Despite, we see a correlation of cortical contractility and cell surface tension, the approach had various weaknesses (see materials and methods section). Values in parenthesis indicate a negative surface tension due to increasing cell surface. Hence, the approach of a cell's surface tension might be wrong in this context.  $p_{\text{con}}^{\text{S}}$  accounts for the fraction of contractile cells generating a contractile stress of at least 0.8 Pa, compensating the external pulling stress.  $E2$  is a measure for the cortical pretension. Cell type + B represents 5  $\mu\text{M}$  blebbistatin treatment. Cell count is given is 2.

Cell line	$\Delta\sigma_{\text{int}}^{\text{S}}$ (mPa s <sup>-1</sup> )	$\sigma_{\text{int}}^{\text{S}}$ (Pa)	$\sigma_{\text{int}}^{\text{R}}$ (Pa)	$\gamma_{\text{CST}}^{\text{R}}$ (pN $\mu\text{m}^{-1}$ )	$p_{\text{con}}^{\text{S}}$ (%)	$E2$ (kPa)
HMEC	321 (77 1853)	1.61 (0.38 9.26)	0.25 (−0.06 0.67)	( $\approx -0.4$ )	63.4	2.9 (0.3 5)
MCF-10A	217 (72 378)	1.09 (0.36 1.89)	0.57 (0.27 0.97)	$\approx 12.9$	58.4	2.5 (0.4 5)
MCF-10A + B	62 (0 156)	0.31 (0.00 0.78)	0.25 (0.12 0.40)	$\approx 1.2$	20.0	0.4 (0.2 3)
MDA-436	29 (0 169)	0.15 (0 0.84)	0.26 (0.08 0.48)	$\approx 2.6$	24.7	0.8 (0.2 5)
MDA-436 + B	11 (0 145)	0.05 (0 0.73)	0.22 (0.09 0.37)	$\approx 1.0$	19.6	0.5 (0.1 4.6)
MDA-231	78 (0 269)	0.39 (0 1.34)	0.24 (0.05 0.52)	( $\approx -1.6$ )	35.1	0.8 (0.2 5)
MDA-231 + B	17 (0 103)	0.08 (0 0.52)	0.17 (0.08 0.27)	$\approx 0.9$	12.9	0.2 (0.1 1.0)
B16	0 (0 20)	0 (0 0.10)	0.43 (0.20 0.69)	( $\approx -29.6$ )	4.8	0.1 (0.2 5)

at the end of stretch  $\sigma_{\text{int}}^{\text{S}}$  was lowered by about 70% (figure 2(b), table 1, figures 18(f) and 22). We defined cells as *strongly contractile* when the cortical contractile stress was larger than the external stretching stress,  $\sigma_{\text{int}}^{\text{S}} > \sigma_{\text{ext}} = 0.8 \text{ Pa}$ . In other words, these cells were able to reverse the deformation curve, bending it down (figure 2(a)). Inhibition of myosin motor activity reduced the fraction of strongly contractile cells from over two-thirds to under one-third (compare table 1).

The blebbistatin treatment did not only affect the deformation during stretch, but also the immediate cortical response ( $E2$ ) and the relaxation after switching off the lasers ( $\sigma_{\text{int}}^{\text{R}}$ ). The pretension  $E2$  was reduced by about 80% (figure 16(c)), which indicates that it is not only an additional passive spring (as suggested by

the SLS model), but rather contributes actively. The contractility *after* stretch  $\sigma_{\text{int}}^{\text{R}}$  was also drastically reduced (figure 2(b) and table 1).

Reduced contractile properties after blebbistatin treatment were consistent for all other cell lines that we analyzed later on (figure 16). On the other hand, the passive viscoelastic cell properties, namely the elasticity ( $E$ ) and viscosity ( $\eta$ ), changed only slightly (figure 16).

Further experiments interfering with the actomyosin functionality were conducted (figure 21). The actomyosin mechanism relies on  $\text{Ca}^{2+}$  [62], which is present in cell culture medium but not in PBS. Consequentially, suspending cells in PBS largely reduced the contractile response. The disruption of actin filaments by the treatment with 250 nM latrunculin A also inhibited cell contractions (figure 21).

We conclude that the actomyosin cortex is responsible for the observed active contraction and refers to it as cortical contractility.

## 2.2. Epithelial cells behave more cortical contractile than mesenchymal cells

Cortical contractile properties are characteristic of epithelial cells and tissues [3, 16, 46, 52, 54]. Recent experiments further revealed a reduction of cortical tension during epithelial–mesenchymal transition (EMT) [18]. In this section, we quantify cortical contractile properties of mesenchymal cells (MDA-MB-436 and MDA-MB-231) and relate them to the epithelial MCF-10A cells.

We found that the mesenchymal cell lines displayed clearly less *cortical* contractile behavior than the epithelial cells (figure 2). This applied to all active contractile parameters ( $\sigma_{\text{int}}^{\text{S}}$ ,  $\sigma_{\text{int}}^{\text{R}}$  and  $E2$ ), which were all statistically significantly lower (see table 1, where also an approximation of cells surface tension (CST) is included).

During stretch, only the epithelial MCF-10A generated an internal contractile stress that was sufficient to overcome the external stretching force, which was clearly visible by the bending of the deformation curve (figure 2(a)). Its contractile stress, during the stretch phase, was calculated to  $\sigma_{10A}^{\text{S}} \approx 1.1$  Pa. The median deformation curves of the mesenchymal cell lines MDA-MB-436 and MDA-MB-231 seem to have predominantly revealed passive creep behavior. Quantitatively, the SLS model quantified that MDA-MB-436 cells actually did contract weakly with a median stress of  $\sigma_{436}^{\text{S}} \approx 0.2$  Pa and MDA-MB-231 cells  $\sigma_{231}^{\text{S}} \approx 0.4$  Pa.

The difference between the epithelial and the mesenchymal cell lines is demonstrated by the respective fractions of strongly contractile cells. In contrast to epithelial cells, where 58% were strongly contractile, only 35% of the MDA-MB-231 and 25% of the MDA-MB-436 mesenchymal cells behave strongly contractile (figure 2(b) and table 1).

In the next step, we focused on the contractility during the relaxation phase ( $\sigma_{\text{int}}^{\text{R}}$ ), which we estimated by the cells' contraction against its viscosity (details are explained in materials and methods). Here, we found again that epithelial MCF-10A cells ( $t > 5$  s in figure 2(a)) were the most contractile cells contracting even below their initial shapes. The mesenchymal cell lines, by contrast, did not contract below their initial shapes ( $\epsilon < 0$  in figure 2(a)), which is in line with a passive relaxation behavior. Moreover, the cortical pretension  $E2$  was much lower for mesenchymal cells than epithelial cells (figure 2(d)).

Both measures of cortical contractility, during stretch as well as relaxation were correlated  $\sigma_{\text{int}}^{\text{S}} \sim \sigma_{\text{int}}^{\text{R}}$  (figure 19(c)). These values reached similar magnitudes (around 1 Pa, see figures 2(b) and (c)).

Additionally, all cell types showed a positive correlation between cortical pretension  $E2$  and contractility during stretch (figure 19(d)). These correlations indicate that distinct cells hold one contractile potential causing the contractile response during and after the stretch and the cortical pretension.

Moreover, we characterized the protein expression profiles of the three cell lines using proteomics (figure 12). Characteristic protein expressions could prove their appropriate usage as representative cell lines for epithelial and mesenchymal phenotype, respectively. To what extent distinctive protein expressions contribute to different contractile behavior remains speculative.

### 2.2.1. Other epithelial and mesenchymal cell lines show similar contractile properties

We hypothesized that strong cortical contractility could be a characteristic property of epithelial cells. To investigate this, we examined human mammary epithelial cells (HMEC) and three additional mouse mesenchymal fibroblast cell lines B16, BALB/3T3, and NIH/3T3. A majority of the epithelial HMEC cells were strongly contractile ( $\sigma_{\text{int}}^{\text{S}} > \sigma_{\text{ext}}$ ). The median cortical contractility ( $\sigma_{\text{int}}^{\text{S}} = 1.6$  Pa) and the cortical pretension ( $E2 \approx 3$  kPa) were even greater than for MCF-10A (figure 18). In contrast, only 5% of the B16 cells were strongly contractile, and the cortical pretension ( $E2 \approx 1$  kPa) was also reduced (figure 18 and table 1). BALB/3T3 and NIH/3T3 cells also showed reduced contractile behavior (figure 21). In summary, this data supports the hypothesis that strong cortical contractility is associated with epithelial cells.

Interestingly, treating epithelial MCF-10A cells with blebbistatin rendered their contractile properties very similar to those of the mesenchymal cell lines. Both the contractility during stretch ( $\sigma_{\text{int}}^{\text{S}}$ ) and the

**Table 2.** Passive rheological parameters of single suspended cells measured in the OS. Values listed are medians and quantiles in parenthesis.  $E$  represents cells' elasticity during stretching. HMEC shows the highest elastic stiffness, and B16 literally zero. All other cells do not show high variance. Thus, even blebbistatin treatment has a minor impact.  $\eta$  gives cells viscosity and is basically similar for all cell types and uninfluenced upon blebbistatin treatment.  $\epsilon(\text{EOS})$  represents general cell deformability. Obviously, highly contractile cell types express low deformability, while passively behaving cell lines are more compliant. This parameter distinctively indicates a major effect of cortical contractility, compared to a minor contribution of passive viscoelastic.  $r$  gives the cell radius in  $\mu\text{m}$  (obtained during 1 s trap period prior cell stretching).  $n$  indicates the amount of examined cells. Cell type + B represents 5  $\mu\text{M}$  blebbistatin treatment.

Cell line	$E$ (Pa)	$\eta$ (Pa s)	$\epsilon(\text{EOS})$ (%)	$r$ ( $\mu\text{m}$ )	$n$
HMEC	60 (81 091)	81 (13 213)	-0.2 (-1.3 0.9)	9.2 (8.4 10.3)	1523
MCF-10A	11 (0 49)	100 (56 204)	0.5 (-0.5 1.5)	8.0 (7.5 8.6)	5566
MCF-10A + B	16 (0 44)	84 (48 145)	1.8 (1.0 2.8)	7.8 (7.3 8.4)	661
MDA-436	14 (0 46)	94 (41 193)	1.8 (0.7 3.1)	7.2 (6.5 7.9)	2953
MDA-436 + B	14 (0 38)	85 (42 161)	2.3 (1.1 3.4)	7.2 (6.5 8.0)	652
MDA-231	22 (0 99)	108 (42 250)	1.0 (0.1 2.1)	8.0 (7.4 8.7)	3955
MDA-231 + B	25 (2 56)	110 (52 211)	1.8 (0.8 2.9)	8.1 (7.5 8.7)	566
B16	0 (0 8)	110 (68 170)	3.4 (2.4 4.5)	7.8 (7.3 8.3)	413

cortical pretension ( $E_2$ ) of blebbistatin-treated cells were quantitatively much closer to the values of the mesenchymal lines (figures 1, 2 and 16). In other words, active cortical contractile properties were distinctively reduced in mesenchymal cells. How these alterations of individual cell behavior affect multicellular properties will be shown below.

### 2.2.2. Cortical contractility is crucial to understand cell rheology

Our applied SLS model (see materials and methods) allows us to infer passive rheological properties such as the elasticity  $E$  and viscosity  $\eta$  (see table 2) at the same time with the active contractile properties (table 1). We observed that implementing active contractions into the model was a crucial to accurately understanding cell rheological response.

The active contraction counteracted the stretching force and thus led to lower deformations. In a passive model, this effect would lead to an overestimation of cell stiffness  $E$ . For instance, MCF-10A cells would appear much harder than the blebbistatin treated MCF-10A cells since they deform much less (figure 2). However, we found that the contractility  $\sigma_{\text{int}}^{\text{S}}$  was the parameter that was most affected by the blebbistatin-treatment, while the elasticity  $E$  and viscosity  $\eta$  remained roughly similar (compare figures 1, 2 and figure 18).

Strikingly, we observed that passive parameters displayed generally lower relative variations compared to active parameters. Stiffness  $E$  and viscosity  $\eta$  differed by a maximum of about 100% and 15%, respectively (see table 2). Compared to these values, the internal cortical contractility during stretch ( $\sigma_{\text{int}}^{\text{S}}$ ) of MCF-10A cells was more than seven times greater than for MDA-MB-436 and almost three times greater than for MDA-MB-231 cells (figure 2 and table 1). Likewise, the contractility during relaxation ( $\sigma_{\text{int}}^{\text{R}}$ ) of MCF-10A was more than twice as strong as compared to both MDA cell lines. The cortical pretension ( $E_2$ ) of epithelial MCF-10A cells was about three times higher than mesenchymal cell lines.

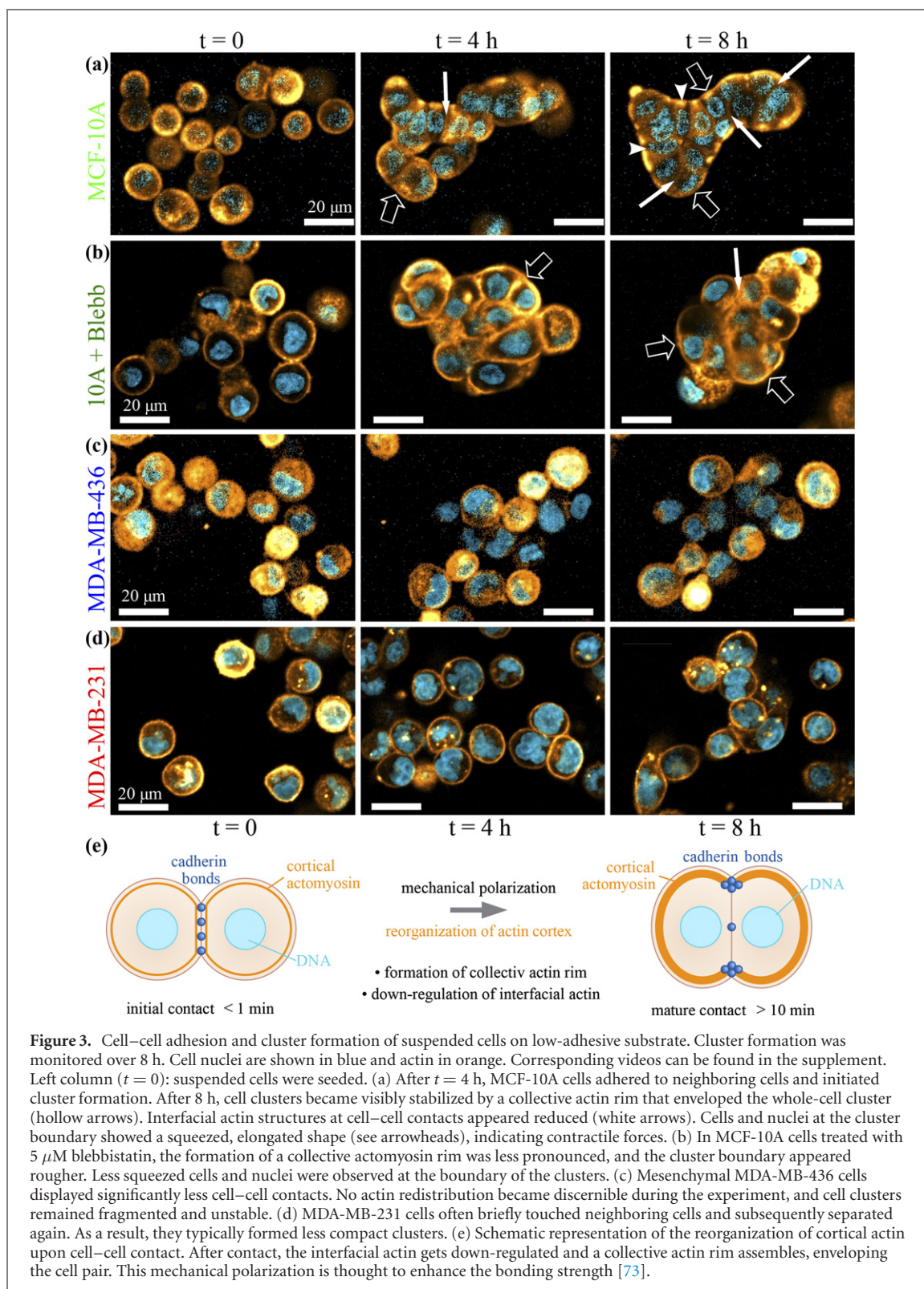
Moreover, high contractility ( $\sigma_{\text{int}}^{\text{S}}$ ) was associated to slight volume contractions of the cells. The two epithelial cell types shrank their volume during the stretch process (figure 17). In other words, these cell lines contracted their short axes such that they overcompensated the stretch along the long axis. Consequentially, their Poisson's ratio  $\nu$  was clearly above 0.5, indicating anomalous material behavior. Hence, cortical contractility seems to squeeze the cells resulting in actively increasing intracellular pressure. Further, this helps to interpret recent results [72]. The Poisson's ratio of the non-contractile cell types (mesenchymal and blebbistatin-treated MCF-10A cells) was between 0 and 0.5 (figure 17).

These results suggest, already on the timescale of seconds, a classification into contractile and non-contractile cell types concerning their cortical properties. Thereby, cortical contractility has the predictable power to discriminate between epithelial and mesenchymal cells.

### 2.3. Cortical contractility contributes to cell–cell clustering

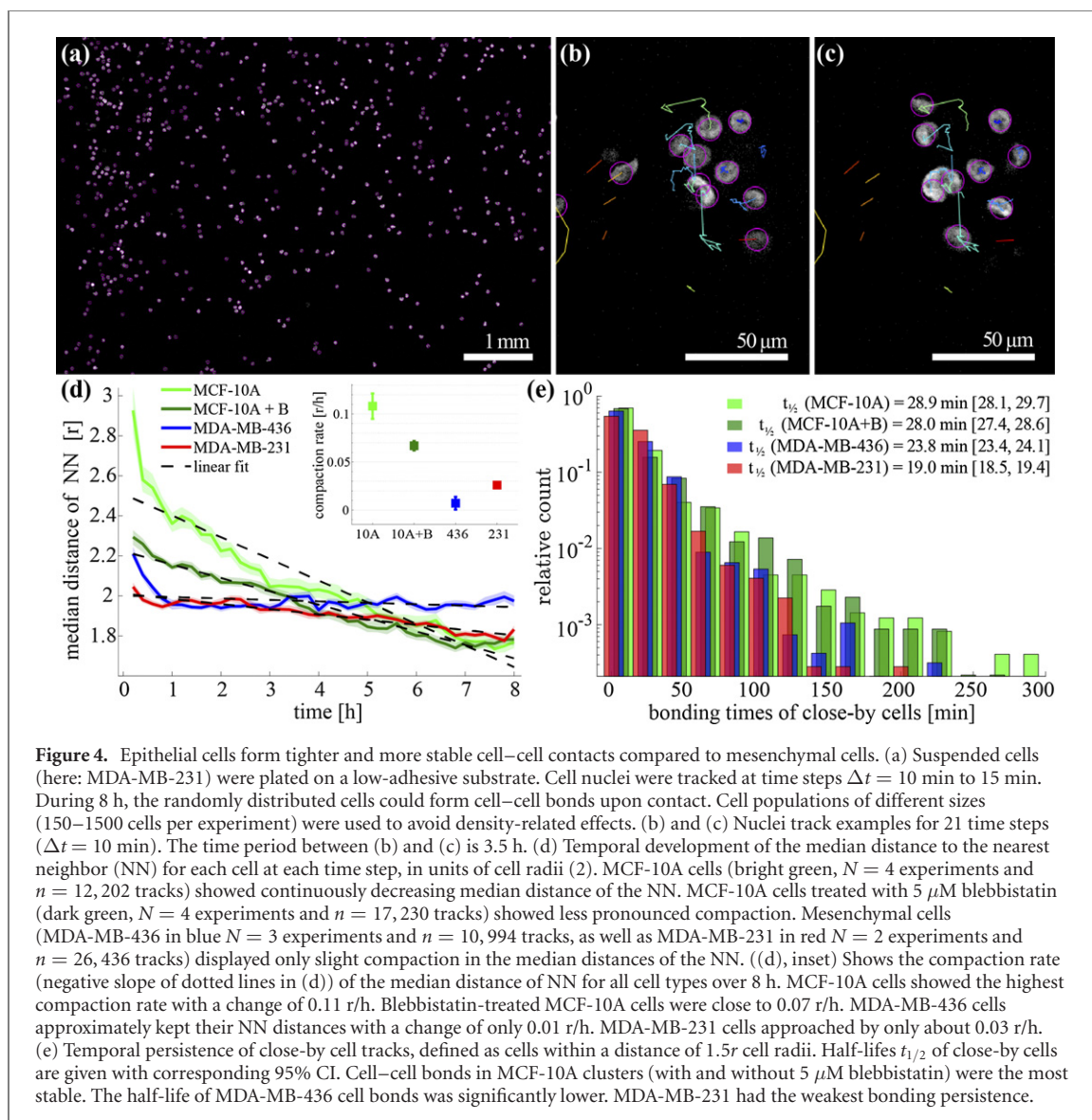
We have found that cortical contractility distinguishes between cell types. In a study by Pawlizak *et al* 2015, the attempt to connect clustering behavior and cell mechanics remained elusive [65]. Here, we investigated whether cortical contractility might influence cell–cell aggregation.

We seeded suspended cells into low-adhesive wells, where they formed interconnected cell clusters with reduced substrate adhesion (figure 3). During the formation of cell–cell contacts, we observed the actin



reorganization (figure 3). We investigated the cell–cell interfaces and the cell–medium interfaces, focusing on forming intercellular collective actin rims that envelop cell clusters.

To quantify the dynamics, we tracked cells during cluster formation. We characterized the development of neighbor distances and stability of neighbor relationships (figure 4). As a measure of cell compaction, we examined the cell–cell distance of the nearest neighbor (NN) of every cell during cluster formation (shown in figure 4(d)). We further determined for every cell a set of *close-by cells* that are located within a distance less than 1.5 cell radii. We characterized the temporal persistence of these close-by cells as a measure for the stability of cell–cell bonds (figure 4(e)).



### 2.3.1. Epithelial MCF-10A cells form stable clusters enveloped by an actin rim

When epithelial MCF-10A cells came into contact with each other, they quickly stuck together. The fluorescence intensity of the cortical actin in the contact area was visibly reduced (figure 3(a), time-lapse videos in SI). It has been proposed that a reduction of cortical tension at cell–cell interfaces, which suggests a mechanical polarization<sup>5</sup>, is crucial for the formation of cell–cell adhesion [4, 16, 73, 74]. The cell clusters form a prominent actin-rich surface enveloping all cells. Besides the smooth surface, squeezed cells and nuclei appeared within the clusters (figure 3(a)), indicating a contractile cluster, which effectively had a high surface tension.

Additionally, our quantitative analysis confirmed the qualitative cluster observations. MCF-10A cells continuously reduced their distance to their respective next neighbor and ultimately reached the highest state of cell compaction (figure 4(d)). The temporal stability of close-by cell pairs was also highest compared to other cell types (figure 4(e)).

The results in cluster formation suggest that cortical contractile mechanisms also play a role here. In the OS, treating MCF-10A cells with blebbistatin reduced the cortical contractility. Thus, we observed how the influence of  $5 \mu\text{M}$  blebbistatin would impact cluster formation. Cluster formation was even faster (figures 3(a) and (b) and supporting videos), potentially due to a reduced cortical pretension (figure 3(e)). However, the formation of an outer collective rim appeared less efficient (figure 3(b)). The cell cluster surface was rougher and seemed less tensed compared to the untreated control. We did not observe squeezed cells and nuclei as a signature of high tissue surface tension (TST). In addition, the compaction

<sup>5</sup> Do not confuse with cell polarization used in other studies to describe directed cell migration. There, a cell fulfills spatial, structural, and functional adaptations to form a leading edge and a rear [1].



rate, which indicates a strong contractile cell adhesion mechanism, was decreased upon myosin inhibition (figure 4(d)). The number/ratio of close-by cells, which is an indicator for the adhesion strength, was only slightly affected by the blebbistatin treatment. Thus, the sustainability of cell–cell bonds was slightly reduced compared to MCF-10A control cells (figure 4(e)). This supports the hypothesis that blebbistatin only reduces the cortical tension/contractility. Hence, cortical contractile cell behavior potentially influences the assembly of cell–cell bonds.

### 2.3.2. Mesenchymal cell lines form less stable cell clusters

Both mesenchymal cell lines MDA-MB-436 and MDA-MB-231 behave qualitatively similar, but completely different compared to epithelial MCF-10A cells. Most obviously, we did not observe that mesenchymal cells formed stable cell–cell contacts (figures 3(c) and (d) and supporting videos). After a brief cell–cell contact, they quickly detached and separated again. We neither observed collective actomyosin rims nor reduced actin cortex intensity at the cell–cell interface (figures 3(c) and (d)).

The tracking analysis confirmed these observations. The median NN distance changed much less during experiments (figure 4(d)), pointing to reduced cell compaction. In MDA-MB-231 cells, the NN distance shrank only by about 10% during the 8 h observation time. MDA-MB-436 approached by only 5%. The overall short median distance between next neighbors of mesenchymal cells (figure 4(d)) was likely caused by frequent NN exchanges. The cell–cell bonds of the mesenchymal cells were also more unstable, since close-by cells were less persistent (figure 4(e) and supporting videos).

In these experiments, we used low-adhesive substrates to avoid cell adhesion to the substrate. Nonetheless, after a few hours, mesenchymal cells preferred the formation of substrate adhesion points in contrast to cell–cell bonds (supplemental videos). This behavior possibly enhances invasive individual cell motility.

In these cluster formation experiments, we have found that the contractile MCF-10A cells formed clusters that seemed to have a higher collective TST. The characteristic footprint of this collective contractile tension were smoother surfaces, squeezed cells and nuclei, a stronger cluster compaction tendency, and more persistent cell–cell contacts. In the cells with lower cortical contractility, some or all of these tendencies appeared to be impaired. Recent theories [73, 75] have suggested that actin redistribution might be crucial for cell–cell contact formation and effectively contributes to TST (figures 3(e) and (g)). This agrees with our findings on epithelial cell clustering. However, an additional effect potentially comes from higher protein expressions of cell–cell adhesion complexes, as catenins, enhancing cell bonds (figure 12).

If these observations scale up also for bigger cell clusters will be examined in the next section.

## 2.4. Cortical contractility influences cell aggregate mechanics

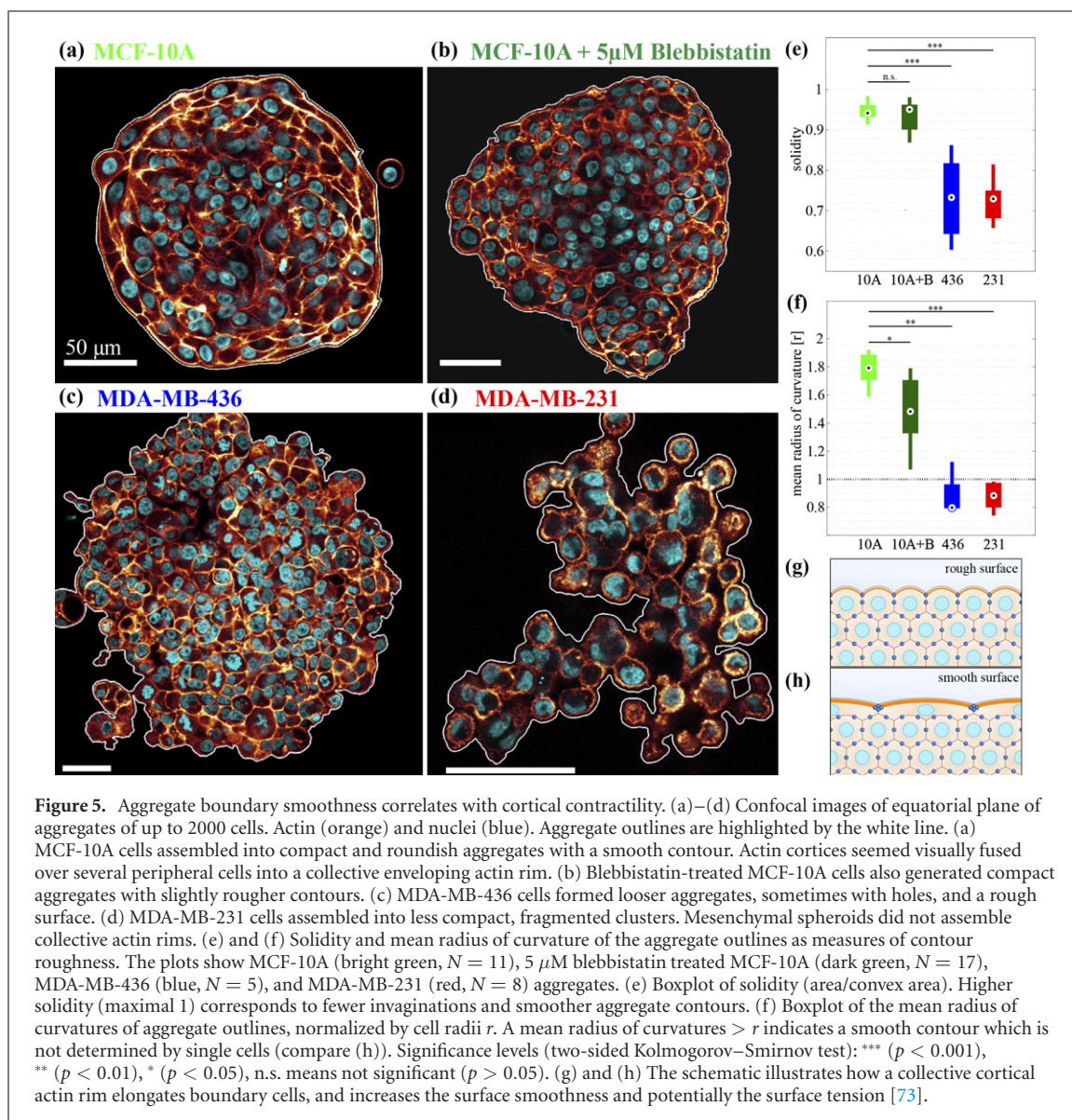
### 2.4.1. Surface appearance of cell aggregates

We have seen that the single-cell contractile behavior was mirrored in the formation of small cell clusters. Subsequently, we related the cortical contractile properties further to the mechanics on tissue scales and built larger multicellular aggregates (in the following just aggregates) up to 2000 cells. During one to two days in a low-adhesive U-well, suspended cells assembled into an aggregate of appropriate size. To examine the aggregates' structure, we fixated, stained, and optically cleared the samples (material and methods). Afterwards, we recorded confocal images to visualize the shapes of the surface and the whole aggregates.

A high TST was thought to lead to a smooth aggregate surface and an overall roundish aggregate shape [65, 73]. To measure this, we first determined the outlines of equatorial confocal sections of the aggregates. We quantified the surface smoothness by (1), the *solidity* of the aggregate outline, which is defined as the ratio of contour area to its convex area, and (2), the outline *radius of curvature* (details are provided in the materials and methods section).

On visual inspection, epithelial MCF-10A aggregates have smooth surfaces, elongated boundary cells, and an overall roundish shape (figure 5(a)). Single cells did not stand out prominently. Instead, the actin cortices seemed to form a collective, continuous rim that extends over several cells. The quantification confirmed these impressions. The outline solidity was close to 1, as would be expected for a roundish aggregate shape without invaginations. The mean radius of curvature of the outline was highest for MCF-10A spheroids (figures 5(e) and (f)). It was greater than the typical single-cell radius  $r$ , which indicates that the aggregate surface shape was not determined by single cells. Since MCF-10A cells express a high cortical contractility compacting small clusters (as shown before), a high contractile surface tension likely generated the smooth surface and elongated cells at the boundary.

To resolve how actin-generated contractile properties affect the contour smoothness of cell clusters, we assembled MCF-10A aggregates in a blebbistatin-containing medium. The general assembly appeared visually similar to untreated aggregates. The contour outlines did not differ very much from untreated aggregates (figure 5(b)). Quantitative analysis revealed no significant differences in the solidity (figure 5(e)).



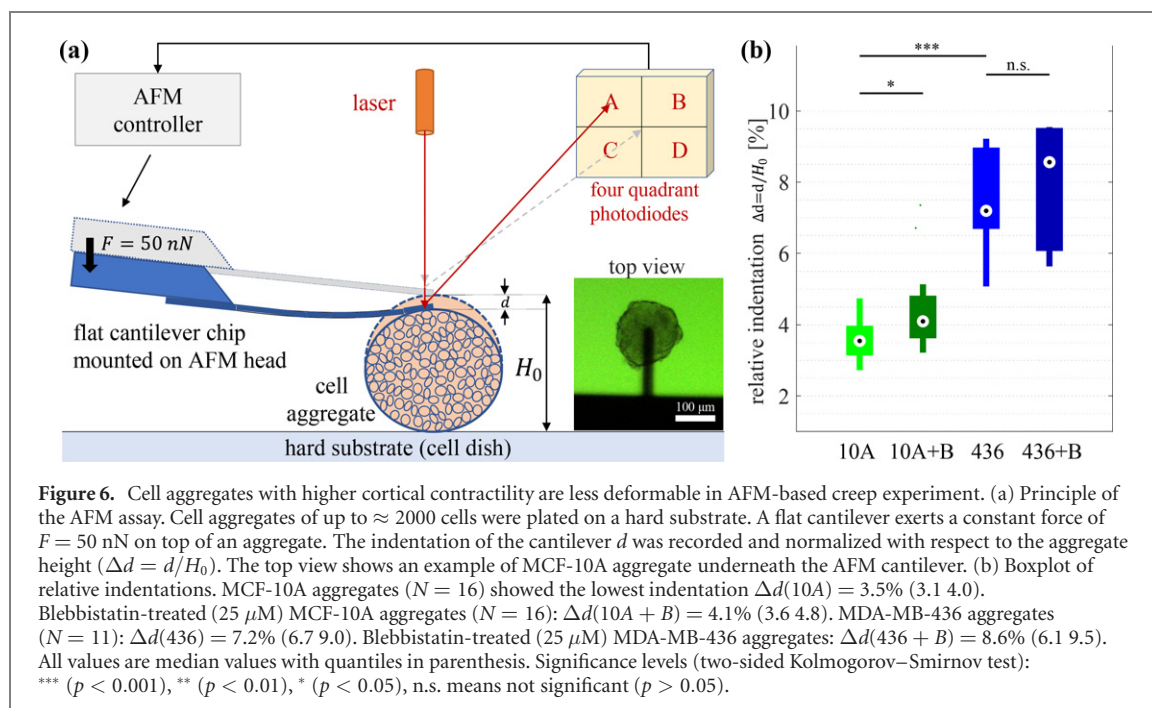
However, boundary cells seemed less elongated and the outline less smooth. Consequentially, the mean radius of curvature was significantly smaller and closer to the typical single-cell radius, which indicates the transition to a grainy outline (figure 5(f)).

These observations support the hypothesis that blebbistatin reduced the emergence of a collective contractile boundary in these aggregates. Hence, cortical contractility likely regulates surface tensile effects.

In contrast to epithelial aggregates, the mesenchymal aggregates of both cell types showed visually a much rougher outline (figure 5). MDA-MB-436 and MDA-MB-231 aggregates (figures 5(c) and (d)) appeared less compact and even showed holes. No collective cortical actin rims were visible. The outline solidity of the mesenchymal aggregates was significantly lower than for MCF-10A, with values of 0.73(0.60.86) for MDA-MB-436 and 0.73(0.660.81) for MDA-MB-231 (figure 5(e)). The mean radius of curvature was even below the average cell radius (figure 5(f)). These parameters characterize a contour with more invaginations whose outline is predominantly determined by single cells. The low solidity and mean radius of curvature points to a reduced surface tension and consequentially in less cohesive strength within the whole spheroid, as observed similarly in [65].

The MDA-MB-231 aggregates that we observed were typically smaller than the clusters of other cell lines. The reason was that already pipetting them disrupted the aggregates, leading to fragmented sub-clusters (figure 5(d)). This behavior suggests weak cell–cell bonds, which was also observed in other studies [65].

Hence, we conclude that the epithelial cells, which hold a high cortical contractile potential, formed aggregates with a collective actin rim and had the smoothest surface among the cell lines that we tested.



Whether these properties correlate to effective aggregate stiffness and/or surface tension will be examined in the following.

#### 2.4.2. Mechanical surface indentations of spheroids correlate with cortical cell contractility

From our previous measurements, we hypothesized that more contractile cells would form stiffer aggregates. We thus probed the resulting mechanical resistance of the aggregates using atomic force microscopy (AFM). The degree of indentation depends on bulk mechanics and on surface tension-like effects [76].

Aggregates were placed underneath a flat AFM cantilever and compressed with a total force of  $F = 50$  nN (figure 6(a)). The cantilever indented the aggregates by less than 10% of their height. To check how contractile properties influence the compliance of aggregates, we compared the relative indentations for MCF-10A aggregates with MDA-MB-436 and inhibited the actomyosin contractility in both cases. For these measurements, we treated the aggregates with  $25 \mu\text{M}$  blebbistatin, shortly (1 h to 2 h) prior to the experiment.

For MCF-10A aggregates the relative indentation increased by about 20% from 3.5% for untreated aggregates to 4.1% for blebbistatin treated aggregates (figure 6(b)). Hence, blocking actomyosin-based contractility resulted in more compliant behavior. Likewise, aggregates from the non-contractile MDA-MB-436 were indented about two times more than MCF-10A (figure 6(b)). Blebbistatin treatment for MDA-MB-436 aggregates showed a tendency to further increase the indentation (figure 6(b)). MDA-MB-231 spheroids could not be measured, since they did not form into sufficiently compacted and stable aggregates, as mentioned before.

In summary, more contractile cell types formed less compliant aggregates. However, these results cannot clearly identify the exact mechanism by which the contractility causes this apparent aggregate stiffness, as several mechanisms are conceivable. First (1), the cortical contractility led to an apparent single-cell stiffness in the OS measurement, directly translating into higher aggregate stiffness. Second (2), the contractile cells tended to compact during aggregate formation, leading to an emergent aggregate stiffness as an indirect consequence of contractility. Third (3), the contractile cells tended to form an (apparent) collective actomyosin rim around aggregates, thus generating an effective TST. This higher TST would, in turn, reduce the aggregate compliance in the AFM.

Together with the results on aggregate surface properties, these results hypothesize that cortical contractility could be associated with a higher effective TST. In the next section, we thus correlate contractility to cell segregation, which is thought to be driven by TST.

#### 2.4.3. Cortical contractility as a driving mechanism for cell segregation

In demixing experiments, cells of different cell types could segregate into distinct compartments that mutually envelope each other. The order of these compartments is a function of an effective TST [55, 65,

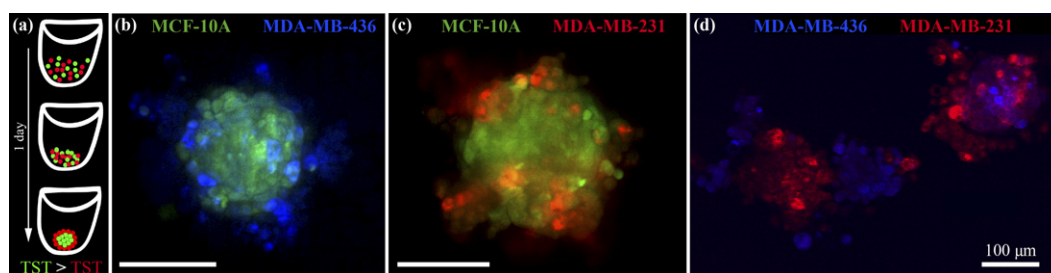


**Figure 7.** Cell segregation as a measure of TST in cell aggregates. (a) Sketch of the demixing assay. Two different suspended cell types ( $\approx 500$  each, previously stained with CellTracker<sup>TM</sup>), were mixed in low-adhesive U-wells. After  $\approx 1$  day cell demixing was evaluated. Aggregates are thought to generate a higher TST when they segregate into the center of the mixture [55, 57]. (b) Epithelial MCF-10A (green) cells always formed an inner core surrounded by mesenchymal MDA-MB-436 (blue) cells ( $N = 10$ ). (c) Epithelial MCF-10A (green) cells also formed an inner core surrounded by mesenchymal MDA-MB-231 (red) cells ( $N = 4$ ). (d) The mixture of the two mesenchymal cell lines resulted in inconsistent, fragmented demixing behavior ( $N = 8$ ).

77, 78]. The tissues with the highest TST ended up forming the innermost compartment. Before, we could not reliably establish a connection between the demixing order and passive biomechanical cell properties [65]. In the cell lines that we investigated here, we found hints of a link between high contractility and high TST in the aggregate compaction dynamics, aggregate surface properties, and aggregate bulk mechanics. These results suggest a demixing order with the strongly contractile epithelial MCF-10A having the highest TST, followed by MDA-MB-436 and then MDA-MB-231.

Respectively, 1000 single cells of two different cell types were stained (CellTracker<sup>TM</sup>) and afterwards intermixed in low-adhesive U-bottom wells. Eventually, after 24 h, we recorded the resulting segregation behavior.

Indeed, MCF-10A cells reproducibly assembled into an inner core when mixed with the mesenchymal MDA-MB-436 or MDA-MB-231 cells (figures 7(b) and (c)). This supports our hypothesis that cortical contractility and the collective contractile rim of the epithelial cells generate a high TST. In contrast, intermixing both mesenchymal cell lines did not lead to reproducible and consistent segregation (figure 7(d)). These results indicate a low and comparable TST for the used mesenchymal cell lines.

In summary, our investigations could consistently connect the single-cell contractility with properties on the aggregate/tissue level, ranging from cell–cell adhesion, cluster dynamics, over surface structure, to aggregate mechanics. So far, we have specifically addressed cortical contractile properties of single cells and cell clusters without substrate adhesions. In the next section, we compare this with stress fiber-based contractility in adhesive environments and emphasize that these are two distinct mechanisms.

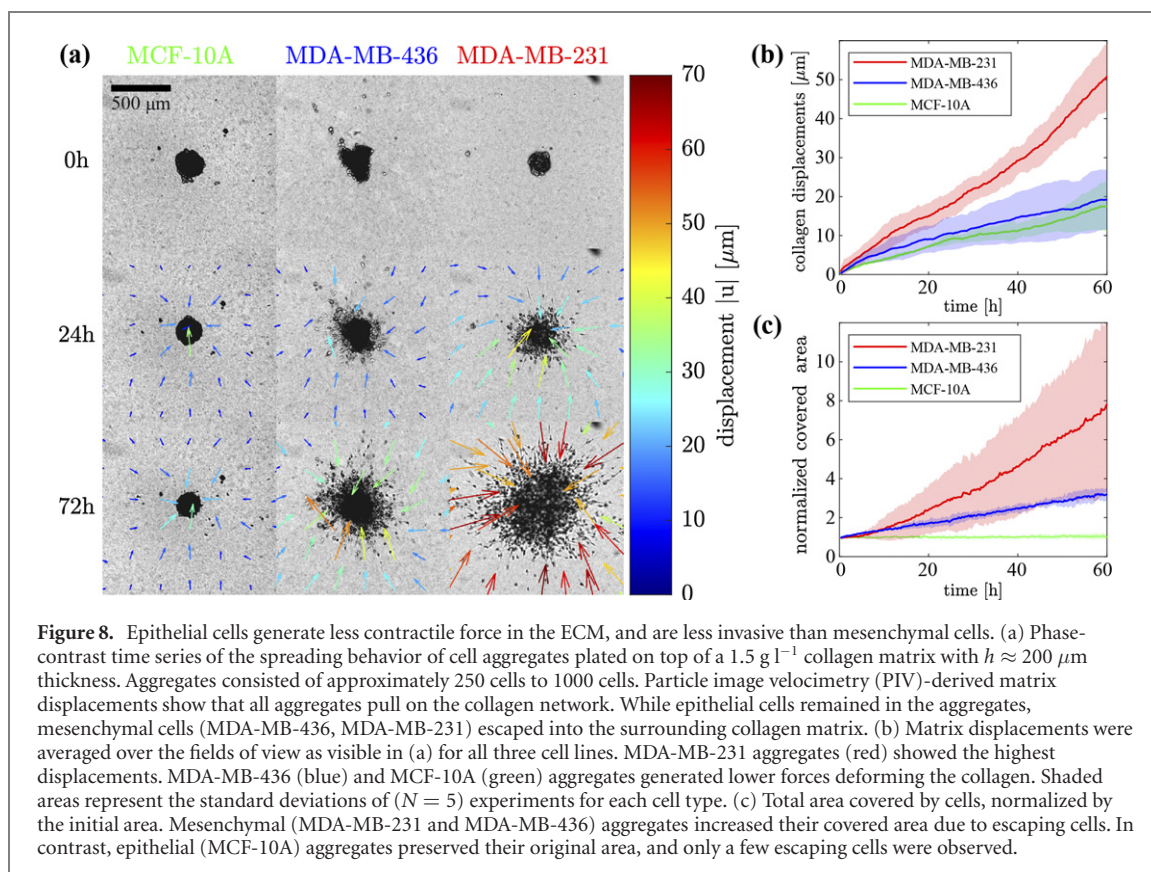
## 2.5. Distinction between substrate-based stress fiber contractility and substrate-independent cortical contractility

### 2.5.1. Stress fiber-based contractility deform collagen networks and foster cell escape

Contractile mechanisms are well-known in both epithelial *and* mesenchymal cell systems, which seems to be in contradiction. Epithelial cells are known to form collective cell layers with prominent actin cables and purse strings on their periphery [19, 79, 80]. Both are known to increase line and surface tension, indicated by concave-shaped boundaries (figure 9(a)) that increase intercellular cohesion and closing wounds [9, 13–15, 17, 79, 81–88]. On the other hand, mesenchymal cells such as MDA-MB-231, also exert highly contractile forces, particularly in adhesive environments like substrates and ECM, which might be crucial for metastasis [21–24, 29, 89, 90].

We thus asked whether the mesenchymal cells that we used would induce higher contractile forces than the epithelial MCF-10A if they were brought in an ECM-based environment. In a simplified 3D traction force microscopy assay, we placed an aggregate onto a collagen matrix. Aggregates were assembled by approximately 1000 MDA-MB-436 or MCF-10A cells, respectively. Since MDA-MB-231 cells hardly form aggregates on their own, we assembled them (approximately 250 cells) through the addition of Matrigel<sup>TM</sup>. All aggregates induced contractile forces that deformed the collagen matrix (figure 8(a)). We recorded the matrix displacements for approximately 60 h and analyzed them using particle image velocimetry (PIV) [91].

We found that the mesenchymal MDA-MB-231 cells induced the highest matrix deformations, indicating that they exert the strongest forces (figure 8(b)). The mesenchymal MDA-MB-436 and the epithelial MCF-10A aggregates created displacements that were comparable with each other. This examination distinguishes whether the collective contractile rim or individual boundary cells dominantly pull on the collagen remains unclear by this examination.



Next, we found that cell escape from the aggregates differed vastly between cell types. To quantify this behavior, we calculated the normalized area covered by cells  $A/A_0$ , with  $A_0$  being the area covered at the beginning of the experiment (figure 8(c)). During the course of the experiment, the epithelial MCF-10A aggregates did not wet the surface and maintained their roundish shape. Only very few individual cells escaped from the aggregates (figures 8(a) and (c)). In contrast, both mesenchymal cell types showed a predominant wetting-like behavior. Many single cells visibly escaped from the original aggregates. After 60 h, the area covered by cells has increased about eight-fold for MDA-MB-231 and about three-fold for MDA-MB-436.

Thus, the high cortical contractility of MCF-10A cells (figure 2) and its collective aggregate formation (figure 3) cannot be associated with pulling forces in the ECM-based assay nor the level of cell escape. Rather, the mesenchymal cell lines exhibited the highest contractility (particularly MDA-MB-231) in the ECM-based assay showed strong wetting-like behavior (MDA-MB-231 and MDA-MB-436). These findings also agree with the literature [21–24, 29, 89]. Taken together, these results suggest that the underlying contractile mechanisms need to be discriminated against. The cortical contractility might be associated with aggregate formation, a collective actin rim, potentially hindering cell escape into the ECM and vice versa protecting epithelial tissues from external invasion. The other type of contractility shows up in environments, where cells form substrate adhesion points and stress fibers driving cell migration and invasion. Stress fibers are known to be contractile in a dipole-like fashion [1, 92], suggesting to term stress-fiber-based contractility.

### 2.5.2. Role of cell contractility in migration on 2D substrates

Many recent research approaches investigated cell migration on 2D substrates and revealed that both cortical actin structures and stress fibers determine specific cell functions such as boundary formation between tissues or enhanced single-cell migration [17, 21, 32, 33, 45, 84, 87, 93]. Hence, we also investigated how the actin structure is organized in cells on regular adhesive substrates and whether we can correlate this to their migration behavior and add to their specific contractility. Based on these approaches, we examined the cell morphology and motility for our three cell lines for 4 h via staining actin and DNA (figure 9). Using fluorescence microscopy, we tracked the cells to characterize their specific motility.

Epithelial MCF-10A cells mostly formed compact islands. Cells on the periphery of the medium frequently generated a collective actin rim as a distinct boundary to the cell–medium interface, similar to the structures observed in aggregates (compare figures 5 and 9). These collective actin cables and purse

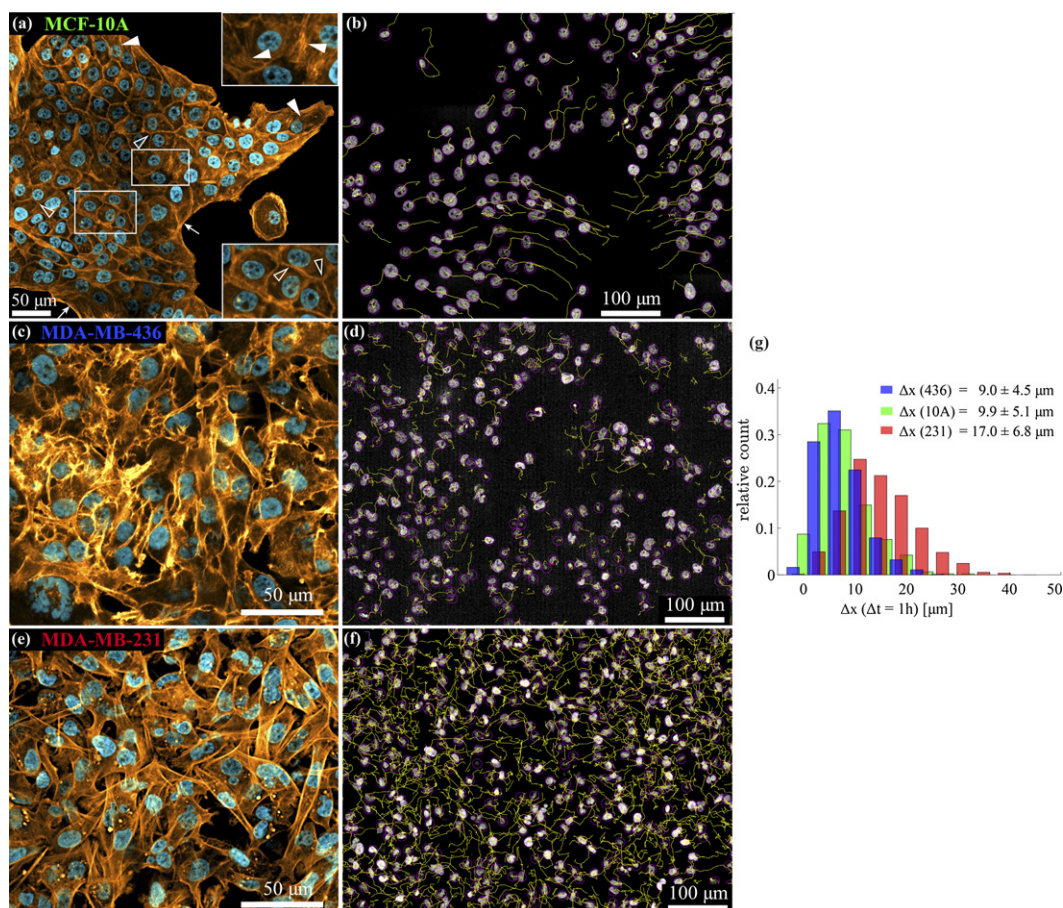


**Figure 9.** Actin morphology on 2D adhesive substrates and corresponding cell motility. Left: snapshots of adhesive cells. Actin is shown in orange and nuclei in blue. Whole time-series and z-stack videos are available as supporting videos. Middle: cell nuclei and tracks over 4 h. (a) Epithelial MCF-10A cells assemble into mono-layers with pronounced actin cortices (lower insert and hollow arrowheads). Actin stress fibers appeared less prominent (upper insert and filled arrowheads). Cells are tightly packed without free space in between. At the boundaries of the cell islands, collective actin cables (arrows) formed, indicating a high line tension. (b) MCF-10A cells showed collective migration behavior indicated by aligned cell tracks. (c) Mesenchymal MDA-MB-436 cells and (e) MDA-MB-231 formed more pronounced actin stress fibers and apparently more elongated cell shapes. Neighboring cells were weakly connected, and no collective interconnecting actin structure was assembled. (d) Tracks of MDA-MB-436 and (f) tracks of MDA-MB-231 revealed that mesenchymal cells migrate randomly and sometimes crawl over each other (compare supporting videos). (g) Typical displacements after 1 h ( $\Delta x = \langle \text{MSD}(\Delta t = 1\text{h}) \rangle^{1/2}$ ). Legend gives mean values  $\pm$  standard deviations. MDA-MB-436 cells ( $n = 744$  tracks) showed similar migration velocities as MCF-10A cells ( $n = 448$  tracks). MDA-MB-231 cells ( $n = 1,460$  tracks) were the fastest cells.

strings, indicated by concave-shaped boundaries, are known to increase line and surface tension and hinder single-cell escape, a behavior that seems to be particularly characteristic of epithelial cell layers [9, 14, 15, 17, 32, 79, 81–88, 94].

When MCF-10A cells were treated with 5  $\mu\text{M}$  blebbistatin, the curved, tensed boundary structures mostly disappeared after already 30 min, and lamellipodial protrusions emerged instead (figures 22(d) and (e)). These results suggest that the intercellular line tension depends on the cortical contractility, supporting our findings from 3D aggregates (figure 5).

In contrast, we observed that mesenchymal cells did not form any compact islands, but rather remained in a disordered, single-cell state. Instead of the collective actin structure, stress fibers were dominant (figures 9 and 10 and corresponding video), which is in line with our proteomic evaluation, where mesenchymal cell lines showed higher expressions of focal adhesion—as well as stress fiber-related proteins (figure 12).

The analysis of the migration behavior showed that MCF-10A cells moved collectively in flock-like packs (see supporting time lapse video and figure 9). In contrast, the motion of the mesenchymal cells was uncorrelated and visibly less persistent. Cells passed by each other, and the layer was unjammed [95–97]. Additionally, they crawled over one another, unlike an epithelial monolayer.

MDA-MB-231 cells were by far the fastest cells with a mean displacement  $\Delta x = \langle \text{MSD}(\Delta t = 1\text{h}) \rangle^{1/2} = (17.0 \pm 6.8) \mu\text{m}$  after 1 h. MCF-10A and MDA-MB-436 displaced approximately half as much (figure 9(g)), indicating that they generated lower traction forces. Interestingly, these forces on 2D substrates correlate

well with the collagen displacements in 3D (figure 8(b)) in several key aspects: displacements were highest in MDA-MB-231 cells while they were comparable for MCF-10A and MDA-MB-436 in both assays, and MCF-10A showed the highest level of collective cell coordination. Hence, these findings support the idea that the counter-play of cortical and stress-fiber-based contractility controls cell motility and escape. These patterns even appeared to be conserved (to a certain degree) across very different environments. Moreover, we found that the presence or absence of collective cortical actin structures was reflected in the motility behavior on substrates. Mesenchymal cells without collective actin structures featured a predominantly individual and unjammed motion, while the collective cortical actin structures in the epithelial MCF-10A cells were associated with collective motility effects.

Our experiments with cell layers on 2D substrates and aggregates in 3D collagen networks showed consistently two distinct contractile mechanisms. In epithelial cells, cortical contractility leads to collective behavior, while for mesenchymal cells, the dipole-like stress-fiber-based contractility appeared to determine their characteristic invasiveness. It has been shown that particularly enhanced actin stress fiber alignment improves cell motility through constrictions [45]. While both mechanisms are contractile, they lead to complementary tissue behavior.

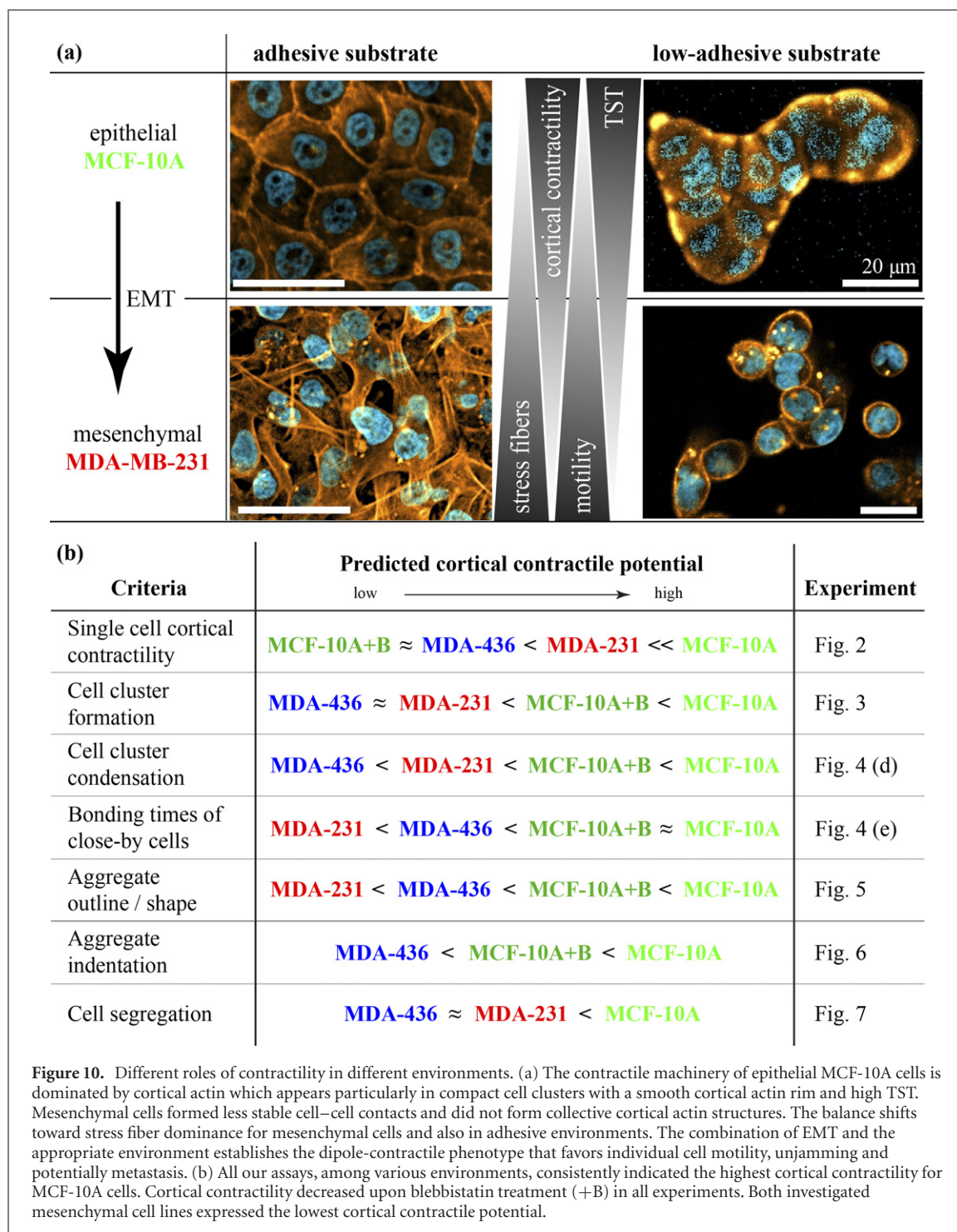
### 3. Discussion

Contractile mechanisms play a crucial role in the collective character of epithelial sheet formation and migration [19, 32, 94]. However, they might also counteract tissue cohesion, drive invasive migration and force generation of single cells and cell clusters in 3D networks. This might be a necessary step in the formation of metastases [21, 23, 25, 29, 98]. Our results help to build a new framework to understand these contrary roles of cell contractility in tissue mechanics. We introduced two distinct, paradigmatic contractile mechanisms that fulfill these respective functions. Cortical contractility stabilizes intercellular cohesion, maintains stable tissue boundaries, and protects the cell from external stresses, which is characteristic of epithelial tissues. By contrast, stress fiber-based dipole-like contractility increases traction forces, which simplifies cell escape and unjamming [21, 45, 97].

The concept of dipole-like contractility has been used before, e.g. in Koch *et al* 2012 [24]. In this study, those single cells that invaded into 3D collagen matrices expressed a dipole-like force profile, while non-invasive cells exerted a more isotropic force profile resembling the cortical contractility mode we found. They showed that the driving factor for ECM invasion was not the force magnitude, but the contractility mode. While these results were restricted to the case of single cells in collagen matrices, we found that the interplay of contrasting modes is a unifying concept that explains tissue behavior across a range of substrates and environments. A study by Ficorella *et al* 2019 showed that the assembly of aligned stress fibers was determining the motility mode of single adhesive cells (even MCF-10A) passing through micro-constrictions [45]. Depending on the cytoskeletal organization, both contractility modes may be employed by the cells. We have summed this up in a  $2 \times 2$  table of pivotal tissue mechanisms as shown in figure 10.

Our results further suggest that the two different types of contractility have opposing effects on the cell shapes and thus result in different jamming and tissue behaviors. This matches the recent observation that traction forces and stress fibers elongate cell shapes and drive shape-dependent unjamming in 2D mono-layers [99]. In our cell lines, the cancerous lines were dominated by stress-fiber responses, which could not only be associated to unjamming in 2D but also to escapes from spheroids into a 3D ECM. More generally, our findings thus suggest a tendency across the environment: stress fiber contractility elongates cells, while cortical contractility counteracts cell elongation and may lead to jammed tissues of roundish cells [9, 19, 20, 73–75, 92, 95, 100–103]. This line of thought applies to dense tissues as in cell jamming. However, it also seems to hold for single cells in the ECM [23, 24, 96, 97]. Our framework thus explains why shape-dependent cell motility occurs in very diverse situations such as cell escape from a tumor (figure 8, [30]), cell squeezing in tumors [103], and in the maintenance of cell order in healthy multicellular systems (figure 3, [20, 79, 95, 104]). Hence, it is likely that pronounced stress fiber assembly plays a decisive role in cell elongation and eventually in the fluidization of malignant tissues.

The concept of two different contractilities might also explain cell segregation experiments that could not solely be explained by passive cell properties such as adhesion and stiffness. In Pawlizak *et al* 2015 [65], they found that these properties did not match the emergent tissue behavior. To determine whether the framework of active contractility, that we found here, would predict tissue behavior better, we have rated the cell lines according to their active cortical contractile behavior (figure 10(b)). To our knowledge, such a nearly fully coherent framework, that links single-cell properties to tissue behavior, has not been established before.



Collective cortical contractility can emerge from single contractile cells by forming an intercellular actomyosin rim. Such an active cortical tension and a collective actin rim have been proposed by the extended differential adhesion hypothesis (eDAH) to resolve the problem of stable cell–cell bonds in tissues, since adhesive forces alone are insufficient to hold tissues together [65, 73, 75, 105, 106]. Hence, active cortical contractility and passive cell–cell adhesion act in concert during the self-organization of stable epithelial tissues. Not only our observations, but a whole range of experiments have emphasized the importance of cortical contractility concerning the eDAH. Epithelial clusters and layers employ contractile mechanisms to generate high surface tension via actin rims that stabilize the aggregates [32, 83–85, 102], increase effective cell–cell cohesiveness [88, 100], enhance wound closure by purse strings [79, 81, 84, 86, 88, 94], delimit compartments and allow laminar transport of air and liquids [2, 13].

To date, it remains difficult to investigate active cortical contractility. Cortical contractile properties cannot easily be detected by traction force microscopy since it is difficult to decouple it from stress-fiber



contractility in adhesive environments. The OS, however, allows to investigate cortical contractility with high throughput independent of the substrate. For instance, an active contractile response of another epithelial cell line was observed by Gyger *et al* 2014 [62]. They related the contractile mechanism to a calcium dependency, which we and others observed as well (figure 21) [8, 107]. Another study by Chan *et al* 2015 applied a similar OS approach and reported cell stiffening upon blebbistatin treatment [108]. Although our cells were more deformable after low-dose blebbistatin treatment, we also computed slightly higher elasticity values with our SLS-model fitting (figure 16). Hence, one must take cortical contractility into account for a meaningful biomechanical characterisation.

Cortical tension was also investigated by AFM approaches [18, 51, 54, 109]. In accordance with our evaluations (figure 16), these previous studies have found a predominant impact on cortical pretension by myosin activity [16, 52], and the cortical tension of epithelial cells was higher compared to mesenchymal cells (figures 2 and 16) [18, 109]. Further, they built multicellular spheroids and correlated cortical properties of the single cell to spheroid assembly. They related higher cortical tension to rounder single cells, especially during mitosis enhancing cancer proliferation [18].

Next to OS and AFM experiments on single cells, a recent study by Notbohm *et al* 2016 revealed the crucial relation between contractility and the global elasticity also in cell monolayers [110]. They concluded that ‘the elasticity is not passive in nature; rather, it is the result of myosin-driven contractility within the cell’ [110]. Consistent with this result, other groups have also found that epithelial cells in mono-layers exert contractile tensions due to cell elongation [82, 83, 90], an effect that we have fully characterized here for the first time in single cells in the OS on the timescale of seconds (figures 16 and 19(b)). Taken together, our results are in agreement with previous studies, which further supports the concept that cortical contractility is central to the rheological response, particularly in epithelial cells.

In order to shed some light on the underlying subcellular processes, we conducted proteomic analyses (figure 12), which brought further insights into the molecular basis of the two specific contractile mechanisms. For instance, actin cross-linker ( $\alpha$ -actinin) was upregulated in MCF-10A cells, while proteins associated with stress-fiber organization (Rac1, Rock2) were downregulated in comparison to both mesenchymal cell lines. Other structure proteins linking the cell membrane to inner cellular structures (radixin, ezrin, catenin) and hence involved in force sensation and transmission were generally upregulated in the epithelial MCF-10A cells. In contrast, proteins crucial for focal adhesions (talin, vinculin) were upregulated in mesenchymal cell lines, which might explain the enhanced tendency of mesenchymal cells to adhere on low-adhesive substrates (see supporting videos). We further found an increased expression of RhoA in MCF-10A cells, while Rac1 and Rock2 expression was lower than in mesenchymal cell lines. While Rac1 plays a role in both contractile aspects, the influence on stress fiber-based contractility seems dominant [111]. Rac1 could thus contribute to the enhanced stress fiber activity in MDA-MB-231 and MDA-MB-436 cells (figure 12). The AFM-based study by Hosseini *et al* 2020 [18] also examined the influence of GTPases. High cortical tension was associated with an increase in RhoA- and a decrease in Rac1 activity, which goes along with our findings (figure 12). The link between protein expression and cell function is not always obvious. Despite this, we found two general tendencies (see figure 12). First, the proteomic data revealed changes in protein expression that are typical for the EMT. Second, we found that the expression of bundling proteins was associated with stress-fiber base mesenchymal cells, while cross-linking proteins favored the organization of a cortex.

To sum up, the importance of cortical contractility in cell and tissue mechanics has been indicated by the scattered evidence of many previous studies [18, 24, 54, 62, 98, 103, 108]. Consistently, our results push beyond these already accepted concepts and highlight for the first time, that it is in fact the interplay of the two different types of contractility that plays a pivotal role in a whole range of effects in tissue mechanics, from single-cell behavior to cluster formation and metastatic potential.

## 4. Materials and methods

### 4.1. Cell culture

All cells were cultured at 37 °C in 5% CO<sub>2</sub> atmosphere. Cell detachment and passaging were done with the help of 0.25 g l<sup>-1</sup> trypsin (Sigma-Aldrich, T4049).

MCF-10A cells are non-tumorigenic epithelial cells, bought from ATCC (CRL-10317). Its culture medium contained a 1 : 1 mixture of Dulbecco’s modified Eagle’s medium and Ham’s F12 medium (PAA E15-813), supplemented with 5% horse serum (H 1270), 20 ng mL<sup>-1</sup> epidermal growth factor (E9644), 10  $\mu$ g mL<sup>-1</sup> insulin (I9278), 100 ng mL<sup>-1</sup> cholera toxin (C8052), 500 ng mL<sup>-1</sup> hydrocortisone (H0396), and 1% Penicillin-Streptomycin (P0781). All components were ordered from Sigma-Aldrich.

**MDA-MB-436** is a malignant mesenchymal (tumorigenic epithelial) cell line bought from ATCC (HTB-130). The culture medium was composed of 89% DMEM (PAA E15-810), 10% Fetal Calf Serum FCS (S 0615) and 1% Penicillin-Streptomycin (P0781). All ordered by Sigma-Aldrich.

**MDA-MB-231** is a metastatic mesenchymal cell line (tumorigenic epithelial-derived from the metastatic site) bought from ATCC (HTB-26). The culture medium was the same as for MDA-MB-436.

**HMEC** (human mammary epithelial cells) were purchased from Thermo Fisher (A10565). The HMEC ready medium was prepared according to the protocol (Thermo Fisher, 12752-010).

**B16-F1** is a mouse melanoma cell line obtained from ATCC (CRL-6323). Culture medium for B16 cells contained 89% Dulbecco's modified Eagle's medium (ATCC, 30-2002), 10% fetal bovine serum (Sigma-Aldrich, PAA A15-102) and 1% Penicillin-Streptomycin (Sigma-Aldrich, P0781).

The **BALB/3T3** clone A31 is a fibroblast and derived from disaggregated 14- to 17 day-old BALB/c mouse embryos obtained from ATCC (CCL-163). Culture medium contained 88% Dulbecco's Modified Eagle's Medium (ATCC, 30-2002), 10% calf serum (Thermo Fisher, 26010074), 1% Penicillin/Streptomycin (Sigma-Aldrich, P0781) and 1% HEPES (Sigma-Aldrich, H4034).

**NIH/3T3** refers to a standard fibroblast cell line established from an NIH Swiss mouse embryo. ATCC provides this cell line (CRL-1658), and they are cultured in the same medium as BALB/3T3.

The segregation hierarchy in Pawlizak *et al* 2015 [65], conducted with the seemingly same cell lines differed from our results (compare figure 7). In their investigation, MDA-MB-436 cells are always sorted in the core in their investigation, indicating they express the highest TST [65]. In contrast, in our experiments, MCF-10A cells always assembled the inner core. Why these ostensible 'identical' cell lines segregate differently remains unclear. We assume biological adaptations during cell cultivation. In our study, cell lines were ordered freshly from ATCC. All our experiments were conducted with cells from the same batch to avoid potential biological and, thus, phenomenological differences. Consequently, our conclusions are drawn exclusively, examining the same cells' response upon different biomechanical assays.

## 4.2. Cell staining

In 2D cultures (low- and high-adhesive), actin was stained with 0.1  $\mu\text{M}$  SiR-actin (Spirochrome, SC001) and the nuclei with 0.18  $\mu\text{M}$  Hoechst-34580 (Molecular Probes, H21486) simultaneously 12 h prior to observation. The stains were kept in cell medium during the whole experiment.

Fixed samples were conserved with 10% formalin (Sigma-Aldrich, HT5011) treated with 1% Triton<sup>TM</sup> X-100 solution (Sigma-Aldrich, 93443). Actin visualization for suspended example cells (figure 1(c)) as well as in aggregates (figure 5) was done with 0.17  $\mu\text{M}$  Alexa Fluor<sup>TM</sup> 532 Phalloidin (Thermo Fisher, A22282). Aggregates were additionally treated by 0.1  $\mu\text{M}$  SiR-DNA (Spirochrome, SC007). Stains were simultaneously added to fixed cells or aggregates, respectively.

Before segregation experiments, the two different cell populations were stained for 1.5 h with 5  $\mu\text{M}$  CellTracker<sup>TM</sup> Green CMFDA (Molecular Probes, C7025) or CellTracker<sup>TM</sup> Red CMTPX (Molecular Probes, C34552), respectively.

## 4.3. Drug treatment

All (–)-**blebbistatin** (Sigma-Aldrich, B0560) treatments had a dose between 5 to 30  $\mu\text{M}$  and were added 30 min to 120 min before experimental investigations for the whole observation time. Exact concentrations and application time are given in the specific results part for all experiments.

**Latrunculin-A** (Sigma-Aldrich, L5163), was added 8 h prior to cell investigations with a concentration of 0.25  $\mu\text{M}$ .

## 4.4. Multicellular aggregates

### 4.4.1. Preparation

Approximately one to two thousand suspended cells were placed in low-adhesive U-bottom wells (Sigma, BR781900). After two days, cells (MCF-10A and MDA-MB-436) self-assembled into one spheroid per well. MDA-MB-231 cells do not self-assemble stable aggregates. However, MDA-MB-231 aggregates could grow with additional 3.5% Matrigel<sup>TM</sup> (Corning<sup>TM</sup> 354234) to the cell medium solution. For collagen experiments with this approach, we resemble the ECM to enable the growth of MDA-MB-231 aggregates.

### 4.4.2. Contour analysis

After fixation and staining (see above), aggregates were cleared with Mounting Medium (ibidi, 50001). Confocal images were recorded using a 63X 1.25 PH3 oil objective on a Leica TCS SP2 confocal laser scanning system in an inverted Leica DM IR2 microscope. Excitation was done with HeNe laser ( $\lambda_{\text{SiR-DNA}} = 633 \text{ nm}$ ) and ArKr laser ( $\lambda_{\text{Phalloidin}} = 514 \text{ nm}$ ).

#### 4.5. Cell segregation experiments

Two different adherent cell lines (for instance, MCF-10A and MDA-MB-231) were individually stained with CellTracker™ red or CellTracker™ green, respectively. Both cultures were then trypsinized, and approximately 1000 suspended cells were transferred, by the same ratio, in low adhesive U-bottom wells (Sigma, BR781900). After one day in segregation medium (1 : 1 mixed by corresponding cell line medium), cells may demix according to their individual arising TST. Aggregates were fixated (see above), and segregation was recorded using an HC PL APO CS 20.0 × 0.70 IMM/COR objective in a Leica TCS SP2 confocal laser scanning system on an inverted Leica DM IR2 microscope. Excitation for the red cells was achieved with a laser wavelength of  $\lambda_{\text{red}} = 543 \text{ nm}$  and for the green ones with a ( $\lambda_{\text{green}} = 488 \text{ nm}$ ).

#### 4.6. Collagen hydrogels

Hydrogels with a final concentration of  $1.5 \text{ g L}^{-1}$  type I collagen were polymerized from a 1 : 2 mixture of rat-tail and bovine skin collagen as described previously [23]. In brief: for 1 mL of the final hydrogel, 125  $\mu\text{L}$  type I rat-tail collagen (Collagen R solution 0.4%, Lot #190193, Serva Electrophoresis, Heidelberg, Germany) and 250  $\mu\text{L}$  type I bovine skin collagen (Collagen G solution 0.4%, Lot #0235G, Biochrom GmbH, Berlin, Germany) were dissolved in 625  $\mu\text{L}$  of a 1M phosphate buffered solution (168  $\mu\text{L}$   $\text{Na}_2\text{HPO}_4$ , 32  $\mu\text{L}$   $\text{NaH}_2\text{PO}_4$ ,  $\text{H}_2\text{O}$  and 425  $\mu\text{L}$  doubled distilled  $\text{H}_2\text{O}$ ). To prevent premature polymerization during the preparation, the process was carried out on the ice, and the collagen solution was immediately transferred into the sample carrier of choice and incubated for 90 min at 37 °C and 95% humidity. Afterwards, the polymerized collagen gels were washed three times with PBS and incubated with the desired cell culture medium.

#### 4.7. Live cell observation

All images and videos were recorded by an inverted Zeiss Axio Observer.Z1 equipped with a Yokogawa CSU-X1A 5000 spinning disk confocal scanning unit Hamamatsu Orca Flash 4.0 camera. The observation chamber was tempered to 37 °C and filled with 5%  $\text{CO}_2$ . Dyes within the cells were excited by 405 nm or 638 nm lasers, to visualize DNA and actin structures.

##### 4.7.1. 2D adherent cells

Cells were cultured and observed in an ibiTreat 96  $\mu$ -well-plate (ibidi, 89626). After two days, confocal images (figure 9) and videos (SI time and z-stack) were recorded. A C-Apochromat 40×/1.2 water immersion objective was used for adherent cell observation. Cell tracking was done with TrackMate [112], analysing the videos where nuclei were stained with 0.18  $\mu\text{M}$  Hoechst-34580 (molecular probes, H21486). Tracks shorter than 1 h were kicked out from further evaluation. Mean square displacement (MSD) was calculated as follows from migration videos with identical frame rates ( $\Delta t = 15 \text{ min}$ ):

$$\text{MSD} \equiv \langle |\mathbf{x}(t) - \mathbf{x}_0|^2 \rangle = \frac{1}{N} \sum_{i=1}^N |\mathbf{x}^{(i)}(t) - \mathbf{x}^{(i)}(0)|^2, \quad (1)$$

where  $\Delta t = 1 \text{ h}$ ,  $N$  is the number of individual tracks (cells), vector  $\mathbf{x}^i(0)$  gives the reference position of the  $i$ th track and  $\mathbf{x}^i(t)$  refers to the position of the  $i$ th cell at time  $t$ .

##### 4.7.2. 2D non-adherent substrate

For investigation of cell cluster assembly, several hundred, previously stained, suspended cells were transferred into uncoated  $\mu$ -well-plate (ibidi, 89621), where cells can hardly adhere (figures 3 and 4). Cell nuclei and their actin structures were recorded immediately, over a wide area (between 12  $\mu\text{m}^2$  to 28  $\mu\text{m}^2$ ) and for at least 8 h. An LD LCI Plan-Apochromat 25×/0.8 glycerin immersion objective was used here.

For evaluation of the NNs, we tracked the nuclei with TrackMate [112], for each time step (10 min to 15 min), compare figures 4(a)–(c). For each cell track, the distance to the nearest cell track was computed for each frame individually. Then, we calculated, at each time point, the median of the distance to the NN of all cell tracks. This median distance to the NN was plotted over all frames for each experiment (distinct well) individually (figure 4(d)). The relative compaction was analyzed as the ratio of the median distance of the NN between the first hour and the last hour. These ratios were calculated for all individual experiments and boxplotted for corresponding cell types. Additionally, the time period of close-by neighbor cells (within a distance of 1.5x of its cell radii) was examined. The ratio of close-by tracks for a certain time period (30 min to 120 min) to all close-by cell tracks was eventually computed and boxplotted (see figure 4(e)).

##### 4.7.3. 3D in collagen hydrogels

In each well of a 24 well  $\mu$ -plate (ibidi, Martinsried, Germany) 250  $\mu\text{L}$  collagen was polymerized as described above. After adequate incubation with cell culture medium, a single spheroid was transferred on

top of each collagen gel. The plate was immediately brought onto an inverted Zeiss axio observer microscope setup with incubation chamber (37 °C, 5% CO<sub>2</sub>) to start the measurement. The assays were recorded over the course of 72 h every 15 min with an EC Plan-Neofluar M27 5×/0.16 objective and an EC-Plan-Neofluar M27 2.5×/0.12 objective in one image plane.

#### 4.8. Quantification of fiber displacement in collagen hydrogels

The collagen displacements were analyzed based on the brightfield images of each time step. We used a custom-written MATLAB script that includes the MATLAB function *imregdemons.m* to detect the displacement of the collagen disregarding the cell movement. The cellular movement is canceled out from each displacement field by applying a mask created with the MATLAB function *entropyfilt.m*. The mean displacement at each time step is calculated as the sum of the cumulative displacements over the complete field of view.

#### 4.9. AFM based indentation experiments of cell aggregates

Two-day-old aggregates were plated into an open cell culture plate and positioned under an AFM scanning head (Nanowizard 4, JPK). After a short time period (30 min to 60 min), aggregates weakly adhered, preventing them from rolling away upon mechanical contact. The cantilever was approached and indented the aggregates with a total force of  $F = 50$  nN. For each spheroid, the indentation was recorded three times and averaged upon these values. Finally, the indentation was normalized with respect to the absolute aggregates height.

#### 4.10. Optical stretcher experiments

For optical stretcher (RS Zelltechnik) experiments, suspended cells were flushed by a microfluidic pump (Fluigent) in the microfluidic system. Phase-contrast images of suspended cells were recorded by an Andor Zyla 5.5 sCMOS camera mounted on an inverted Zeiss Axio Observer Z1 and an LD Plan-Neofluar 63×/0.75 Korr Ph 2 M27 objective. Single suspended cells were trapped  $P_{\text{trap}} = 100$  mW 1 s in between two opposing divergent infrared laser beams (Fibolux Fibotec,  $\lambda = 1064$  nm). Afterwards the laser power during stretching was increased up to  $P^S = 875$  mW, inducing an optical stress of  $\sigma_{\text{ext}}^S \approx 0.8$  Pa acting on the cell surface and an energy absorption, increasing the effective temperature of the cell to  $T_{\text{eff}} \approx 37$  °C. The cell deformation was recorded for 5 s upon laser application. Subsequently, the laser power was switched back to  $P^R = 100$  mW, holding the cell stable to record its relaxation behavior for 15 s. In the end, the cell was flushed away, and a new cell was trapped and measured by the same laser pattern. Cell shape data were automatically calculated by a sub-pixel accurate edge detection algorithm programmed in Matlab (MathWorks). For details, see [57–59, 66, 67]. The algorithm corrects for small-angle rotations of the trapped cell. However, the evaluation dismisses cells rotating more than 20°. Several thousand cells were evaluated regarding cell area, long- and short-axis, and elliptic deformation and averaged median values. Moreover, single-cell deformations were investigated to uncover viscoelastic rheological properties.

##### 4.10.1. Quantification of passive- and active viscoelastic cell properties

With an automated OS device, we investigated cells' rheological responses. Here, we introduce a novel quantification method to characterize both passive and active cell mechanical properties simultaneously. In brief, we fitted a SLS as a Kelvin representation [113, 114] to every single cell's strain curve. In this way, we obtained viscoelastic properties such as *shear viscosity* ( $\eta$ ), *elastic modulus* ( $E$ ) and *cortical pretension* ( $E_2$ ). Since the optical stretch stimulus seems to induce a cumulative active contractile cell response, we added a linear contractile term (*cortical contractile stress during the stretch* (S)  $\sigma_{\text{int}}^S$ ) counteracting external stress stimuli, compare figure 11. Hence, we analyzed the creep behavior with a decreasing effective external stress, where the decreasing factor defines the contractile stress ( $\sigma_{\text{eff}} = \sigma_{\text{ext}} - \Delta\sigma_{\text{int}}^S t$ ) as a first order Taylor approximation.  $\Delta\sigma_{\text{int}}^S$  represents the contractile stress compare figure 11. The internal contractile stress is the accumulation during a stretch phase of  $t^S = 5$  s ( $\sigma_{\text{int}}^S = \Delta\sigma_{\text{int}}^S * t^S$ ), which we account for in the entire paper as *internal contractile stress*, during stretch. We define cells behaving as *strongly contractile*, when their internal contractile stress exceeds external applied stress ( $\sigma_{\text{int}}^S > 0.8$  Pa  $\approx \sigma_{\text{ext}}$ ). Hence, cells show decreasing deformation at the end of the stretch.

Unfortunately, the SLS model cannot describe cells' relaxation behavior. Hence, we quantified cells' active contractility after laser application in a different way. Since cells relax passively with an almost purely elastic drop when optical stress ceases, we dismissed half a second of the relaxation time for our further quantification. Hence, we decoupled passive relaxation (disregard in further evaluation) with active contractile relaxation, which we accounted for. The cells' relaxation behavior was mostly linear contractile (see figures 1(a) and 11(a)). We assumed that the cells are solely fluid materials that linearly contracts under constant contractile stress. In this case, the internal contractile stress, ( $\sigma_{\text{int}}^R$ , during relaxation (R)) is

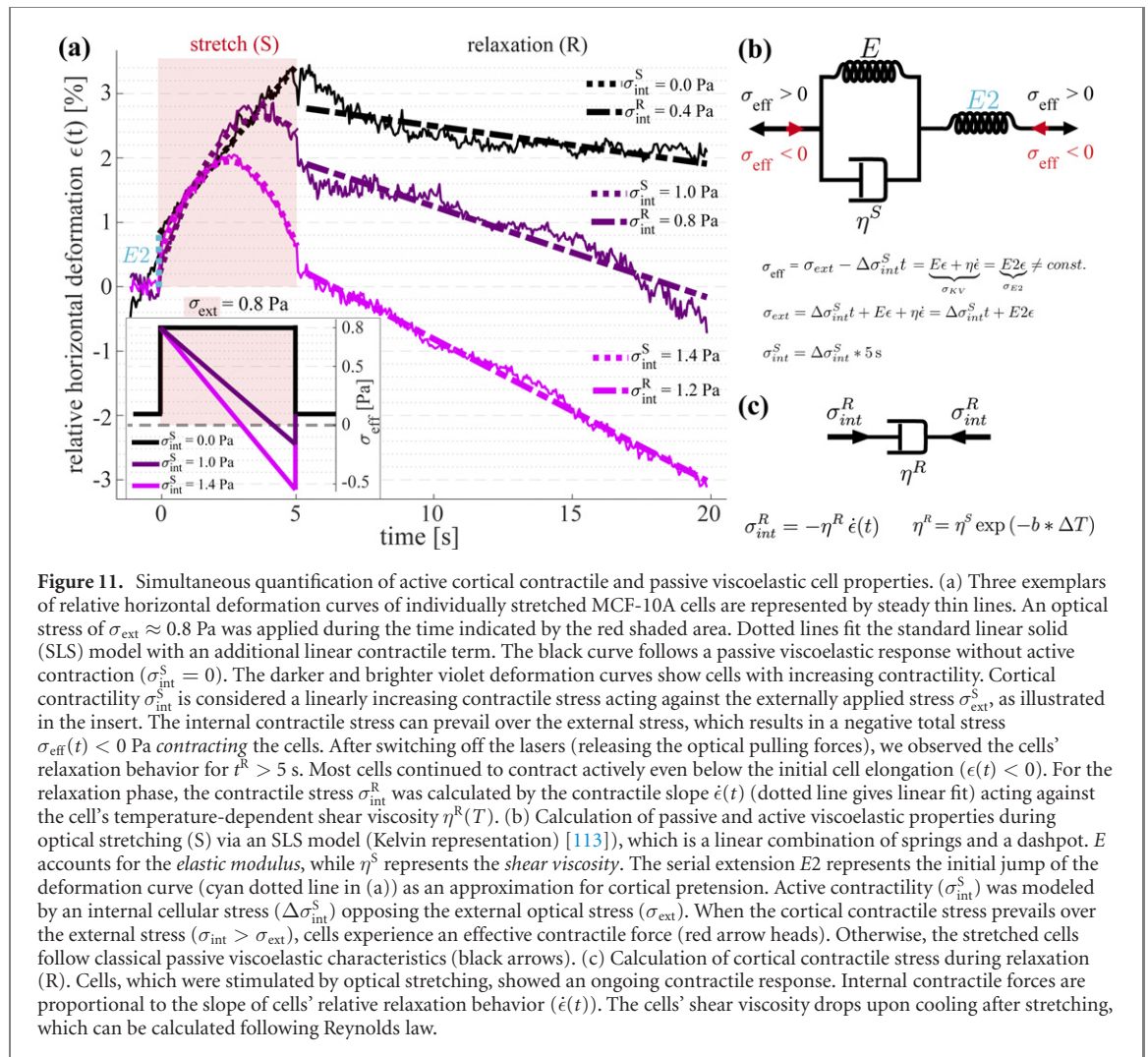


**Figure 11.** Simultaneous quantification of active cortical contractile and passive viscoelastic cell properties. (a) Three exemplars of relative horizontal deformation curves of individually stretched MCF-10A cells are represented by steady thin lines. An optical stress of  $\sigma_{\text{ext}} \approx 0.8 \text{ Pa}$  was applied during the time indicated by the red shaded area. Dotted lines fit the standard linear solid (SLS) model with an additional linear contractile term. The black curve follows a passive viscoelastic response without active contraction ( $\sigma_{\text{int}}^S = 0$ ). The darker and brighter violet deformation curves show cells with increasing contractility. Cortical contractility  $\sigma_{\text{int}}^S$  is considered a linearly increasing contractile stress acting against the externally applied stress  $\sigma_{\text{ext}}^S$ , as illustrated in the insert. The internal contractile stress can prevail over the external stress, which results in a negative total stress  $\sigma_{\text{eff}}(t) < 0 \text{ Pa}$  contracting the cells. After switching off the lasers (releasing the optical pulling forces), we observed the cells' relaxation behavior for  $t^R > 5 \text{ s}$ . Most cells continued to contract actively even before the initial cell elongation ( $\epsilon(t) < 0$ ). For the relaxation phase, the contractile stress  $\sigma_{\text{int}}^R$  was calculated by the contractile slope  $\dot{\epsilon}(t)$  (dotted line gives linear fit) acting against the cell's temperature-dependent shear viscosity  $\eta^R(T)$ . (b) Calculation of passive and active viscoelastic properties during optical stretching (S) via an SLS model (Kelvin representation) [113], which is a linear combination of springs and a dashpot.  $E$  accounts for the elastic modulus, while  $\eta^S$  represents the shear viscosity. The serial extension  $E2$  represents the initial jump of the deformation curve (cyan dotted line in (a)) as an approximation for cortical pretension. Active contractility ( $\sigma_{\text{int}}^S$ ) was modeled by an internal cellular stress ( $\Delta\sigma_{\text{int}}^S$ ) opposing the external optical stress ( $\sigma_{\text{ext}}$ ). When the cortical contractile stress prevails over the external stress ( $\sigma_{\text{int}} > \sigma_{\text{ext}}$ ), cells experience an effective contractile force (red arrow heads). Otherwise, the stretched cells follow classical passive viscoelastic characteristics (black arrows). (c) Calculation of cortical contractile stress during relaxation (R). Cells, which were stimulated by optical stretching, showed an ongoing contractile response. Internal contractile forces are proportional to the slope of cells' relative relaxation behavior ( $\dot{\epsilon}(t)$ ). The cells' shear viscosity drops upon cooling after stretching, which can be calculated following Reynolds law.

proportional to the slope of the contractile deformation. That means:  $\sigma_{\text{int}}^R = \eta^R(T)\dot{\epsilon}(t)$ , where  $\eta^R(T)$  is the cellular shear viscosity during relaxation. Since the shear viscosity  $\eta(T)$  is temperature-sensitive, the model also includes thermal alterations upon laser exposure and release. In fact, according to Reynolds law, the shear viscosity of single suspended cells in OS devices drops by approximately 10% upon 1 K temperature increase [66]. Optical stretching with 875 mW heats up the cell by  $\approx 17 \text{ K}$  yielding physiological conditions of an effective temperature about  $T_{\text{eff}} \approx 37^\circ \text{C}$ . Hence, we exploited the relation:  $\eta^R(\Delta T) = \eta^S e^{(-b\Delta T)}$ , where  $\eta^S$  is the cells shear viscosity during stretching (fitted by SLS model),  $b$  gives the change rate of shear viscosity (here  $b = 0.1 \equiv 10\% \text{ per Kelvin}$ ),  $\Delta T$  represents the absolute temperature change (here  $\Delta T \approx 17 \text{ K}$ ), to obtain the increased shear viscosity of cells during relaxation. Further implications of thermal effects on contractility are discussed in the next section and in supporting figures 13–15.

Finally, the fitting curves match the measured irregular deformation curves surprisingly well, justifying our approach. Passive creep compliance is overlaid by active contractility. For short application times (stretching below 2 s, compare supplemental figure 20), active cell contraction might not be visible in observed data due to the retarded response of the contraction mechanism. However, cells are prestressed, and the contractile reaction can drastically alter curve shapes and could result in the misinterpretation of the cell's rheological properties when the data are described with solely passive viscoelastic properties. Hence, we generally suggest applying a passive viscoelastic creep model (e.g. SLS) with an implemented active contractile parameter, as introduced here. The model does not represent actual cytoskeletal structures, and its contributions to viscoelastic or contractile deformations allow an unbiased view of its origin.

The following notation was used:

- $\sigma_{\text{ext}} = 0.8 \text{ Pa}$ —is the optical stress acting on the cell surface upon an optical laser power of  $LP = 875 \text{ mW}$ , for details compare calculations in [62]. However, in supplemental data figures 13, 20 and 21 different external stresses were applied.

- $\Delta\sigma_{\text{int}}^{\text{S}}$  (Pa s<sup>-1</sup>)—is the rate of cortical contractility a suspended cells gains due to external stimuli. Our model suggests a linear increase upon optical stretching.
- $\sigma_{\text{int}}^{\text{S}}$  Pa—is the total contractile stress after 5 s stretch period. Hence,  $\sigma_{\text{int}}^{\text{S}} = \Delta\sigma_{\text{int}}^{\text{S}} * 5 \text{ s}$ .
- $\sigma_{\text{int}}^{\text{R}}$  Pa—is the internal contractile stress leading to cortical contraction during relaxation.
- $\sigma_{\text{KV}}$ —gives the exerted stress upon the Kelvin–Voigt arm.
- $\sigma_{\text{E2}}$ —is the exerted stress upon the additional serial spring.
- $\epsilon(t)$ —the strain represents cell deformation upon external stress  $\sigma_{\text{ext}}$  and potentially induced internal contractile stress  $\sigma_{\text{int}}$ .
- $E$  (Pa)—represents the elasticity of single suspended cells within our SLS model.
- $\eta$  (Pa s)—is the shear viscosity of a cell.
- $E2$  (Pa)—represents a serially aligned elastic modulus reflecting the instantaneous response to cell stretch. In a biomechanical view, it determines the total cortical stiffness of a cell's actomyosin cortex and combines the contribution of both active pretension and passive cross-linking. Our analysis indicates its main contribution to active pretension due to a distinct drop in  $E2$  upon blebbistatin treatment, see supporting figure 16(c).
- $\tau[1/\text{s}] = \eta/E$ .

For creep curve fitting following relations were used:

$$\sigma(t) = \sigma_{\text{ext}} - \Delta\sigma_{\text{int}}^{\text{S}}t = \underbrace{E\epsilon + \eta\dot{\epsilon}}_{\sigma_{\text{KV}}} = \underbrace{E2\epsilon}_{\sigma_{\text{E2}}} \neq \text{const.} \quad (2)$$

$$\sigma_{\text{ext}} = \Delta\sigma_{\text{int}}^{\text{S}}t + E\epsilon + \eta\dot{\epsilon} = \Delta\sigma_{\text{int}}^{\text{S}}t + E2\epsilon \quad (3)$$

$$\epsilon(t) = \epsilon_{\text{KV}} + \epsilon_{\text{E2}}. \quad (4)$$

Solving these differential equations leads to the following strain dependence, which was used for fitting the individual creep curves:

$$\epsilon(t) = \frac{1}{E} \left[ (\sigma_{\text{ext}} - \Delta\sigma_{\text{int}}^{\text{S}}t + \Delta\sigma_{\text{int}}^{\text{S}}\tau) - (\sigma_{\text{ext}} + \Delta\sigma_{\text{int}}^{\text{S}}\tau) \exp\left(-\frac{t}{\tau}\right) \right] + \frac{\sigma_{\text{ext}} - \Delta\sigma_{\text{int}}^{\text{S}}t}{E2}. \quad (5)$$

For a passive model, where the internal contractile stress is zero ( $\Delta\sigma_{\text{int}}^{\text{S}} = 0$ ), which was used for short stretches of only 2 s (see supporting figures 20 and 21), the solution is calculated as:

$$\epsilon(t) = \frac{\sigma_{\text{ext}}}{E} \left[ 1 - \exp\left(-\frac{t}{\tau}\right) \right] + \frac{\sigma_{\text{ext}}}{E2}. \quad (6)$$

The 2D images of suspended cells recorded during optical stretching experiments provide us with the horizontal and vertical axes for all frames. An approximation of a cell as a prolate spheroid quantifies the cell volume during the whole stretching process.

$$V_{\text{cell}} = \frac{4}{3}\pi h v^2, \text{ where } h \text{ represents horizontal – and } v \text{ the vertical elongation, respectively.} \quad (7)$$

The relative volume change can be approximated by

$$\Delta V_{\text{cell}}(t) = V_0 \left( 1 + \frac{\Delta h(t)}{h_0} + 2 \frac{\Delta v(t)}{v_0} + \dots \right), \quad (8)$$

where  $V_0$ ,  $h_0$ ,  $v_0$  indicates the initial volume, horizontal and vertical elongation, while  $V(t)$ ,  $h(t)$ ,  $v(t)$  represents the time dependent volume, horizontal and vertical elongation, respectively. We calculated the median change of cell volume for each cell type by averaging the last ten frames (0.5 s) at the end of stretch (EOS) and compared it with the corresponding initial cell volume ( $dV_{\text{EOS}}$ ).

While other studies have linked contractility to CST [18, 52, 54], we believe that a straightforward derivation is not easy due to a number of reasons. First, the calculation of a CST assumes the conservation of the cell volume, but we observed slight cell compression during cell contraction (figure 17). Second, other energies involved in this deformation were neither considered. An appropriate calculation considering cell compression and further energy changes, would exceed the scope of this paper. Nonetheless, we have used the method described below to estimate the CST, but have not included this result in the main section due to the aforementioned reasons. We focused only on the relaxation process, where only contractile forces apply and are not superimposed by external pulling forces as it is the case during the stretching process. In general, surface tension is defined as the change of surface energy over the change of surface area:

$\gamma_{\text{CST}} = \frac{dE}{dA}$ , where the change of surface energy is the contractile force ( $F$ ) times the absolute deformation

(de). Cells surface area ( $A$ ) was approximated as an prolate spheroid, where the horizontal axis ( $h$ ) from our individual suspended cells, corresponds to the long axis, and our vertical axis ( $v$ ) determines both short axis in the calculation:

$$A_{\text{cell}} = 2\pi v^2 \left( 1 + \frac{h}{ve} \arcsin e \right), \text{ where } e^2 = 1 - \frac{v^2}{h^2}. \quad (9)$$

$\gamma_{\text{CST}}^{\text{R}} = F \frac{d\epsilon}{dA}$ , where  $F$  is cells internal contractile force,  $d\epsilon$  is the change of absolute elongation, and  $dA$  accounts for the change in cells absolute surface area (all during relaxation).

However, during the evaluation, we see cell types increasing their surface area. Hence, this effect is not explainable with a surface tension minimizing its surface area. Since we approximate the spatial surface area via only a 2D projection, it is very likely to miscalculate the surface area. Even due to minimal alterations of the surface area during relaxation, which increases the potential error.

Values in parenthesis indicate a negative surface tension due to increased cell surface. Hence the approach of a cell's surface tension might be difficult in this context.

#### 4.10.2. Thermal influence on cells contractility upon optical stretching

To prevent potential misinterpretations of gained contractile properties, we additionally analyzed heating effects during optical stretching. Recent studies revealed a significant temperature increase in the OS, reducing cells viscosity, which results in enhanced cell deformability [66, 68]. Simultaneously, higher temperature increases contractility due to enhanced single myosin efficiency according to the Arrhenius law [115]. Decoupling these interfering effects, we compared firstly various optical forces at similar effective temperatures (supplemental figure 14) and secondly similar applied force at different effective temperatures (supplemental figure 15). The first revealed, higher optical stress induced higher contractility, see supplemental figure 14. This indicates that the observed contractility is more mechanosensitive and less thermosensitive. In the second, we observed a thermal threshold when stretching with similar forces an increasing effective temperatures, see supplemental figure 15. In fact, beyond  $T_{\text{eff}} > 40$  °C, the motor protein based mechanism involved in the actomyosin contraction seems to lose its functionality. However, the contractile mechanism seems reversible since, after stress release, the effective temperature rapidly drops back to  $T_{\text{eff}}^{\text{R}} \approx 20$  °C and the contractile mechanism became functional again, see also supplemental figures 13 and 20.

Additionally, we compared the contractile response during relaxation between long (5 s) and short (2 s) stretch stimuli. We quantified about half of the contractile stress after only half of the stimulation time. For instance, for MCF-10A cells upon 5 s stretch we evaluated  $\sigma_{\text{int}}^{\text{R}} = 0.6$  Pa and for the same cells upon 2 s stretch:  $\sigma_{\text{int}}^{\text{R}} = 0.3$  Pa, the internal contractile stress was only half (compare figures 2 and 21 for 800 mW). Similar behavior show HMEC cells. After 5 s optical stress  $\sigma_{\text{int}}^{\text{R}} = 0.25$  Pa, and after short stretch application  $\sigma_{\text{int}}^{\text{R}} = 0.1$  Pa (compare figures 2 and 21 for 800 mW).

Despite these efforts, we could not fully decouple mechanical and thermal stimuli since both effects depend on the laser power. Our results indicate that mechano-responsive effects than temperature-induced more drive observed cortical contractility. Altogether, the underlying mechanism of activating myosin motors and thus cortical contractility scales with induced optical stress, effective temperature, and application time (see supporting figures 13–15, 20).

Despite considerable heating within the OS, its analytical advantages prevail potential artifacts upon thermal alterations. Suspended cells in the OS are independent of their microenvironment without any mechanical contact influencing their contractile force distribution, which is not the case in approaches such as AFM or micropipette aspiration approaches [115, 116]. Thermal alterations within OS experiments were already investigated and indicated only influences on passive viscoelastic properties within physiological temperatures [66, 68] and disturbed only active properties beyond physiological temperatures [69, 117], which we discerned as well (figure 15). However, if thermal stimuli are crucial for cortical contractions, we observed mechanical distinctions of contractile properties within our cell types and conclude their mechanical impact upon cell–cell assembly and tissue formation. Their origin is not the focus of this survey.

#### 4.11. Quantitative proteomics

Proteomic analysis was carried out using stable isotope labeling in cell culture (SILAC) and liquid chromatography-mass spectrometry (LS-MS/MS). An in-depth quantitative analysis protocol is provided in previous publications [118–121]. All experiments were conducted with five biological replicates without any technical replicates. In brief, proteomic labeling was achieved by nurturing cell lines MCF-10A, MDA-MB-231, and MDA-MB-436 with stable isotopically labeled amino acids with different nucleotide masses (SILAC approach). Corresponding medium for MCF-10A cells was prepared with unlabeled 0.1 mg L-arginine/0.1 mg l-lysine/ml ('light'-weight isotopes), for MDA-MB-436 cells with 0.1 mg

[13C6]-L-arginine/0.1 mg [2H4]-L-lysine/ml ('medium'-weight isotopes), and for MDA-MB-231 cells with 0.1 mg [13C6/15N4]-L-arginine/0.1 mg [13C6/15N2]-L-lysine/ml ('heavy'-weight isotopes). All SILAC amino acids were purchased from Thermo Fisher Scientific GmbH and added with each medium change twice per week. Cells were cultivated at least seven days before analysis to ensure at least 95 percent incorporation of isotopically labeled amino acids. Cells of the biological replicates were washed and lysed with 6 M urea, 2 M thiourea, and protease inhibitor (Roche, Mannheim, Germany). Sample handling of the biological replicates and the whole-cell extracts are in detail described elsewhere [120]. Protein lysates of all whole-cell extract triplets, i.e. 'light', 'medium', and 'heavy' labeled lysates, were equimolarly mixed before separation by 1D-SDS-PAGE and prepare for LC-MS/MS [121]. Protein concentrations were subsequently quantified by BCA protein assay (Pierce, Rockford, IL, USA). For protein identification, MaxQuant ([www.maxquant.org](http://www.maxquant.org)) was used described in detail elsewhere [118]. All protein quantifications of all biological replicates were median normalized. Differentially expressed SILAC-ratios were subsequently calculated for all five triplets of MCF-10A, MDA-MB-231, and MDA-MB-436, e.g. ratio MCF-10A/MDA-MB-231. Proteins quantified in three out of five replicates were considered quantified. SILAC-ratios follow a ratio distribution  $p(X/Y)$  with  $X$  and  $Y$  being random variables representing the quantified protein expression of two isotope-labeled cell extracts, e.g. cell extracts of 'light' MCF-10A and 'heavy' MDA-MB-231. The random variables  $X$  and  $Y$  are assumed uncorrelated, noncentral normal distributed. The exact ratio distribution can be found elsewhere [122]. The mean of ratios was calculated and corrected for statistical errors according to [122, 123]. Well-suited approximations can be found elsewhere [124, 125]. All ratios are log 2-plotted. In total, we identified 3954 intracellular proteins, of which 2678 were reliably quantified in at least three of the five biological replicates. For our analysis, we selected the actin-related proteins as presented in figure 12.

### Author contributions statement

EW conceived, conducted, and analyzed all experiments, if not mentioned differently. SG conceived experiments with low adhesive substrates and helped to quantify the data. EB executed and analyzed all collagen assays, while FS gave initial ideas. RS conceived and conducted stretcher experiments with 2 s exposure time. XX conducted and analyzed AFM experiments. JMT conducted the quantitative proteomics, HK evaluated them and MB supervised these experiments. JS and JAK supervised the project. EW wrote the manuscript and all authors reviewed it.

### Conflict of interest

The authors declare no competing interests.

### Acknowledgments

We like to thank Lisa Manning for inspiring discussions, Tobias R Kießling for writing the image analysis for OS data evaluation, Erik Morawetz for implementing further features, Steve Pawlizak for graphical contributions, and Pablo Gottheil for help in data analysis. This work was supported by the European Research Council (ERC-741350), the European Union's Horizon 2020 (668039, FORCE), and the DFG (267494027, INST 268/296-1 FUGG).

### Data availability statement

The data that support the findings of this study are available upon reasonable request from the authors.

### ORCID iDs

Enrico Warmt  <https://orcid.org/0000-0002-3422-2563>  
Steffen Grosser  <https://orcid.org/0000-0002-6863-9607>  
Xiaofan Xie  <https://orcid.org/0000-0003-4842-6134>  
Hans Kubitschke  <https://orcid.org/0000-0002-6019-325X>  
Frank Sauer  <https://orcid.org/0000-0003-2718-6338>  
Jörg Schnauß  <https://orcid.org/0000-0002-6408-8676>  
Josef A Käs  <https://orcid.org/0000-0003-3158-2480>



## References

- [1] Huber F, Schnauß J, Röncke S, Rauch P, Müller K, Fütterer C and Käs J 2013 Emergent complexity of the cytoskeleton: from single filaments to tissue *Adv. Phys.* **62** 1–112
- [2] Alberts B et al 2002 *Molecular Biology of the Cell* 4th edn (New York: Garland Science)
- [3] Schierbaum N, Rheinlaender J and Schäffer T E 2019 Combined atomic force microscopy (AFM) and traction force microscopy (TFM) reveals a correlation between viscoelastic material properties and contractile prestress of living cells *Soft Matter* **15** 1721–9
- [4] Smeets B, Cuvelier M, Pešek J and Ramon H 2019 The effect of cortical elasticity and active tension on cell adhesion mechanics *Biophys. J.* **116** 930–7
- [5] Trepats X and Sahai E 2018 Mesoscale physical principles of collective cell organization *Nat. Phys.* **14** 671–82
- [6] Paul S et al 2008 Convergence and extension at gastrulation require a myosin IIB dependent cortical actin network *Development* vol 135 (Cambridge: Cambridge University Press) pp 2435–44
- [7] Maître J-L, Turlier H, Illukkumbura R, Eismann B, Niwayama R, Nédélec F and Hiiragi T 2016 Asymmetric division of contractile domains couples cell positioning and fate specification *Nature* **536** 344–8
- [8] Coravos J S, Mason F M and Martin A C 2017 Actomyosin pulsing in tissue integrity maintenance during morphogenesis *Trends Cell Biol.* **27** 276–83
- [9] Canty L, Zarour E, Kashkooli L, François P and Fagotto F 2017 Sorting at embryonic boundaries requires high heterotypic interfacial tension *Nat. Commun.* **8** 157
- [10] Murrell M, Oakes P W, Lenz M and Gardel M L 2015 Forcing cells into shape: the mechanics of actomyosin contractility *Nat. Rev. Mol. Cell Biol.* **16** 486–98
- [11] Lange J R and Fabry B 2013 Cell and tissue mechanics in cell migration *Exp. Cell Res.* **319** 2418–23
- [12] Chan C J et al 2019 Hydraulic control of mammalian embryo size and cell fate *Nature* **1**
- [13] Salomon J et al 2017 Contractile forces at tricellular contacts modulate epithelial organization and monolayer integrity *Nat. Commun.* **8** 13998
- [14] Sakar M S, Eyckmans J, Pieters R, Eberli D, Nelson B J and Chen C S 2016 Cellular forces and matrix assembly coordinate fibrous tissue repair *Nat. Commun.* **7** 11036
- [15] Anon E, Serra-Picamal X, Hersen P, Gauthier N C, Sheetz M P, Trepats X and Ladoux B 2012 Cell crawling mediates collective cell migration to close undamaged epithelial gaps *Proc. Natl Acad. Sci.* **109** 10891–6
- [16] Chugh P and Paluch E K 2018 The actin cortex at a glance *J. Cell Sci.* **131** jcs186254
- [17] Ajeti V et al 2019 Wound healing coordinates actin architectures to regulate mechanical work *Nat. Phys.* **15** 696
- [18] Hosseini K, Taubenberger A, Werner C and Fischer-Friedrich E 2020 EMT-induced cell-mechanical changes enhance mitotic rounding strength *Adv. Sci.* **7** 2001276
- [19] Brugués A et al 2014 Forces driving epithelial wound healing *Nat. Phys.* **10** 683–90
- [20] Heller E and Fuchs E 2015 Tissue patterning and cellular mechanics *J. Cell Biol.* **211** 219–31
- [21] Mierke C T 2019 The matrix environmental and cell mechanical properties regulate cell migration and contribute to the invasive phenotype of cancer cells *Rep. Prog. Phys.* **82** 064602
- [22] Mierke C T, Rösel D, Fabry B and Bräbek J 2008 Contractile forces in tumor cell migration *Eur. J. Cell Biol.* **87** 669–76
- [23] Fischer T, Wilharm N, Hayn A and Mierke C T 2017 Matrix and cellular mechanical properties are the driving factors for facilitating human cancer cell motility into 3D engineered matrices *Converg. Sci. Phys. Oncol.* **3** 044003
- [24] Koch T M, Münster S, Bonakdar N, Butler J P and Fabry B 2012 3D traction forces in cancer cell invasion *PLOS ONE* **7** e33476
- [25] Kraning-Rush C M, Califano J P and Reinhart-King C A 2012 Cellular traction stresses increase with increasing metastatic potential *PLOS ONE* **7** e32572
- [26] Yilmaz M and Christofori G 2009 EMT, the cytoskeleton, and cancer cell invasion *Cancer Metastasis Rev.* **28** 15–33
- [27] Kumar S and Weaver V M 2009 Mechanics, malignancy, and metastasis: the force journey of a tumor cell *Cancer Metastasis Rev.* **28** 113–27
- [28] Kim J et al 2017 Stress-induced plasticity of dynamic collagen networks *Nat. Commun.* **8** 842
- [29] Ouderkerk J L and Krendel M 2014 Non-muscle myosins in tumor progression, cancer cell invasion, and metastasis *Cytoskeleton* **71** 447–63
- [30] Iliina O et al 2020 Cell–cell adhesion and 3D matrix confinement determine jamming transitions in breast cancer invasion *Nat. Cell Biol.* **22** 1103–115
- [31] Lee J M, Dedhar S, Kalluri R and Thompson E W 2006 The epithelial–mesenchymal transition: new insights in signaling, development, and disease *J. Cell Biol.* **172** 973–81
- [32] Vedula S R K, Hirata H, Nai M H, Brugués A, Toyama Y, Trepats X, Lim C T and Ladoux B 2014 Epithelial bridges maintain tissue integrity during collective cell migration *Nat. Mater.* **13** 87–96
- [33] Friedl P and Gilmour D 2009 Collective cell migration in morphogenesis, regeneration and cancer *Nat. Rev. Mol. Cell Biol.* **10** 445–57
- [34] Wang W Y et al 2019 Actomyosin contractility-dependent matrix stretch and recoil induces rapid cell migration *Nat. Commun.* **10** 1
- [35] Savagner P 2001 Leaving the neighborhood: molecular mechanisms involved during epithelial–mesenchymal transition *BioEssays* **23** 912–23
- [36] Thiery J P and Sleeman J P 2006 Complex networks orchestrate epithelial–mesenchymal transitions *Nat. Rev. Mol. Cell Biol.* **7** 131–42
- [37] Kubitschke H, Schnauss J, Nnetu K D, Warmt E, Stange R and Kaes J 2017 Actin and microtubule networks contribute differently to cell response for small and large strains *New J. Phys.* **19** 093003
- [38] Ananthakrishnan R et al 2005 Modelling the structural response of an eukaryotic cell in the optical stretcher *Curr. Sci.* **88** 1322
- [39] Rheinlaender J, Wirbel H and Schäffer T E 2021 Spatial correlation of cell stiffness and traction forces in cancer cells measured with combined SICM and TFM *RSC Adv.* **11** 13951–6
- [40] Gardel M L, Schneider I C, Aratyn-Schaus Y and Waterman C M 2010 Mechanical integration of actin and adhesion dynamics in cell migration *Annu. Rev. Cell Dev. Biol.* **26** 315–33

- [41] Schnauß J, Golde T, Schuldt C, Schmidt B U S, Glaser M, Strehle D, Händler T, Heussinger C and Käs J A 2016 Transition from a linear to a harmonic potential in collective dynamics of a multifilament actin bundle *Phys. Rev. Lett.* **116** 108102
- [42] Schnauß J, Händler T and Käs J A 2016 Semi-exible biopolymers in bundled arrangements *Polymers* **8** 8
- [43] Tojkander S, Gateva G and Lappalainen P 2012 Actin stress fibers—assembly, dynamics and biological roles *J. Cell Sci.* **125** 1855–64 Publisher: The Company of Biologists Ltd Section: Commentary
- [44] Svitkina T 2018 The actin cytoskeleton and actin-based motility *Cold Spring Harbor Perspect. Biol.* **10** a018267
- [45] Ficorella C, Martínez Vázquez R, Heine P, Lepera E, Cao J, Warmt E, Osellame R and Käs J A 2019 Normal epithelial and triple-negative breast cancer cells show the same invasion potential in rigid spatial confinement *New J. Phys.* **21** 083016
- [46] Salbreux G, Charras G and Paluch E 2012 Actin cortex mechanics and cellular morphogenesis *Trends Cell Biol.* **22** 536–45
- [47] Berk A et al 2016 *Molecular Cell Biology* vol 8 (New York: Macmillan Learning)
- [48] Strehle D, Schnauß J, Heussinger C, Alvarado J, Bathe M, Käs J and Gentry B 2011 Transiently crosslinked F-actin bundles *Eur. Biophys. J.* **40** 93–101
- [49] Lorenz Jessica S et al 2018 Synthetic transient crosslinks program the mechanics of soft, biopolymer-based materials *Adv. Mater.* **30** 1706092
- [50] Levayer R and Lecuit T 2012 Biomechanical regulation of contractility: spatial control and dynamics *Trends Cell Biol.* **22** 61–81
- [51] Chugh P et al 2017 Actin cortex architecture regulates cell surface tension *Nat. Cell Biol.* **19** 689–97
- [52] Fischer-Friedrich E, Hyman A A, Jülicher F, Müller D J and Helenius J 2014 Quantification of surface tension and internal pressure generated by single mitotic cells *Sci. Rep.* **4** 6213
- [53] Harvey L et al 2000 *Molecular Cell Biology* 4th edn (San Francisco, CA: Freeman)
- [54] Fischer-Friedrich E, Toyoda Y, Cattin C J, Müller D J, Hyman A A and Jülicher F 2016 Rheology of the active cell cortex in mitosis *Biophys. J.* **111** 589–600
- [55] Steinberg M S 1963 Reconstruction of tissues by dissociated cells *Science* **141** 401–8
- [56] Harris A K 1976 Is cell sorting caused by differences in the work of intercellular adhesion? A critique of the Steinberg hypothesis *J. Theor. Biol.* **61** 267–85
- [57] Guck J et al 2005 Optical deformability as an inherent cell marker for testing malignant transformation and metastatic competence *Biophys. J.* **88** 3689–98
- [58] Seltmann K et al 2013 Keratins significantly contribute to cell stiffness and impact invasive behavior *Proc. Natl Acad. Sci.* **201310493**
- [59] Yang T, Bragheri F and Minzioni P 2016 A comprehensive review of optical stretcher for cell mechanical characterization at single-cell level *Micromachines* **7** 90
- [60] Guck J, Ananthakrishnan R, Mahmood H, Moon T J, Cunningham C C and Käs J 2001 The optical stretcher: a novel laser tool to micromanipulate cells *Biophys. J.* **81** 767–84
- [61] Gresser S, Fritsch A W, Kießling T R, Stange R and Käs J A 2015 The lensing effect of trapped particles in a dual-beam optical trap *Opt. Express* **23** 5221
- [62] Gyger M, Stange R, Kießling T R, Fritsch A, Kostelnik K B, Beck-Sickingler A G, Zink M and Käs J A 2014 Active contractions in single suspended epithelial cells *Eur. Biophys. J.* **43** 11–23
- [63] Nel I, Morawetz E W, Tschodu D, Käs J A and Aktas B 2021 The mechanical fingerprint of circulating tumor cells (CTCs) in breast cancer patients *Cancers* **13** 1119
- [64] Fritsch A, Höckel M, Kiessling T, Nnetu K D, Wetzel F, Zink M and Käs J A 2010 Are biomechanical changes necessary for tumour progression? *Nat. Phys.* **6** 730–2
- [65] Steve P et al 2015 Testing the differential adhesion hypothesis across the epithelial–mesenchymal transition *New J. Phys.* **17** 083049
- [66] Kiessling T R et al 2013 Thermorheology of living cells—impact of temperature variations on cell mechanics *New J. Phys.* **15** 045026
- [67] Schnauß J, Käs J A and Smith D M 2017 Contact-free mechanical manipulation of biological materials *Springer Handbook of Nanotechnology* ed B Bhushan (Berlin: Springer) pp 617–41
- [68] Schmidt B U S, Kießling T R, Warmt E, Fritsch A W, Stange R and Käs J A 2015 Complex thermorheology of living cells *New J. Phys.* **17** 073010
- [69] Chan C J, Whyte G, Boyde L, Salbreux G and Guck J 2014 Impact of heating on passive and active biomechanics of suspended cells *Interface Focus* **4** 20130069
- [70] Huster C et al 2020 Stretching and heating cells with light—nonlinear photothermal cell rheology *New J. Phys.* **22** 085003
- [71] Schnauß J et al 2021 Cells in slow motion: apparent undercooling increases glassy behavior at physiological temperatures *Adv. Mater.* **33** 2101840
- [72] Mokbel M, Hosseini K, Aland S and Fischer-Friedrich E 2020 The Poisson ratio of the cellular actin cortex is frequency dependent *Biophys. J.* **118** 1968–76
- [73] Amack J D and Manning M L 2012 Knowing the boundaries: extending the differential adhesion hypothesis in embryonic cell sorting *Science* **338** 212–5
- [74] Hidalgo-Carcedo C, Hooper S, Chaudhry S I, Williamson P, Harrington K, Leitinger B and Sahai E 2011 Collective cell migration requires suppression of actomyosin at cell–cell contacts mediated by DDR1 and the cell polarity regulators Par3 and Par6 *Nat. Cell Biol.* **13** 49–59
- [75] Lisa Manning M et al 2010 Coaction of intercellular adhesion and cortical tension specifies tissue surface tension *Proc. Natl Acad. Sci.* **107** 12517
- [76] Guillaume L et al 2019 Characterization of the physical properties of tumor-derived spheroids reveals critical insights for pre-clinical studies *Sci. Rep.* **9** 6597
- [77] Steinberg M S 2007 Differential adhesion in morphogenesis: a modern view *Curr. Opin. Genet. Dev.* **17** 281–6
- [78] Beysens D A, Forgacs G and Glazier J A 2000 Cell sorting is analogous to phase ordering in fluids *Proc. Natl Acad. Sci.* **97** 9467–71
- [79] Vedula S R K et al 2015 Mechanics of epithelial closure over non-adherent environments *Nat. Commun.* **6** 6111
- [80] Phuong Le A et al 2021 Adhesion-mediated heterogeneous actin organization governs apoptotic cell extrusion *Nat. Commun.* **12** 1–18
- [81] Danjo Y and Gipson I K 1998 Actin purse string filaments are anchored by E-cadherin-mediated adherens junctions at the leading edge of the epithelial wound, providing coordinated cell movement *J. Cell Sci.* **111** 3323–32

- [82] Mertz A F, Banerjee S, Che Y, German G K, Xu Y, Hyland C, Marchetti M C, Horsley V and Dufresne E R 2012 Scaling of traction forces with the size of cohesive cell colonies *Phys. Rev. Lett.* **108** 198101
- [83] Vincent R, Bazellieres E, Pérez-González C, Uroz M, Serra-Picamal X and Trepat X 2015 Active tensile modulus of an epithelial monolayer *Phys. Rev. Lett.* **115** 248103
- [84] Klarlund J K 2012 Dual modes of motility at the leading edge of migrating epithelial cell sheets *Proc. Natl Acad. Sci.* **109** 15799–804
- [85] Chen T et al 2019 Large-scale curvature sensing by directional actin flow drives cellular migration mode switching *Nat. Phys.* **15** 393
- [86] Vasioukhin V and Fuchs E 2001 Actin dynamics and cell–cell adhesion in epithelia *Curr. Opin. Cell Biol.* **13** 76–84
- [87] Adam S et al 2018 Supracellular contraction at the rear of neural crest cell groups drives collective chemotaxis *Science* **362** 339–43 Publisher: American Association for the Advancement of Science Section: Report
- [88] Nnetu K D, Knorr M, Käs J and Zink M 2012 The impact of jamming on boundaries of collectively moving weak-interacting cells *New J. Phys.* **14** 115012 Bristol: IOP Publishing
- [89] Yamada K M and Sixt M 2019 Mechanisms of 3D cell migration *Nat. Rev. Mol. Cell Biol.* **20** 738–52
- [90] Oakes P W, Banerjee S, Marchetti M C and Gardel M L 2014 Geometry regulates traction stresses in adherent cells *Biophys. J.* **107** 825–33
- [91] Thielicke W and Stamhuis E 2014 PIVlab—towards user-friendly, affordable and accurate digital particle image velocimetry in MATLAB *J. Open Res. Software* **2** 1
- [92] Vicente-Manzanares M, Ma X, Adelstein R S and Horwitz A R 2009 Non-muscle myosin II takes centre stage in cell adhesion and migration *Nat. Rev. Mol. Cell Biol.* **10** 778–90
- [93] Dey S and Das M 2021 Differences in mechanical properties lead to anomalous phase separation in a model cell co-culture *Soft Matter* **17** 1842
- [94] Paul H et al 2021 Anomalous cell sorting behavior in mixed monolayers discloses hidden system complexities *New J. Phys.* **23** 043034
- [95] Bi D et al 2016 Motility-driven glass and jamming transitions in biological tissues *Phys. Rev. X* **6** 021011
- [96] Blauth E et al 2021 Jamming in embryogenesis and cancer progression *Front. Phys.* **9** 445
- [97] Oswald L, Grosser S, Smith D M and Käs J A 2017 Jamming transitions in cancer *J. Phys. D: Appl. Phys.* **50** 483001
- [98] Friedl P, Locker J, Sahai E and Segall J E 2012 Classifying collective cancer cell invasion *Nat. Cell Biol.* **14** 777–83
- [99] Saraswathibhatla A and Notbohm J 2020 Traction and stress fibers control cell shape and rearrangements in collective cell migration *Phys. Rev. X* **10** 011016
- [100] Cavey M and Lecuit T 2009 Molecular bases of cell–cell junctions stability and dynamics *Cold Spring Harbor Perspect. Biol.* **1** a002998
- [101] Yamada S and Nelson W J 2007 Localized zones of Rho and Rac activities drive initiation and expansion of epithelial cell–cell adhesion *J. Cell Biol.* **178** 517–27
- [102] George A et al 2016 Dynamic myosin activation promotes collective morphology and migration by locally balancing oppositional forces from surrounding tissue *Mol. Biol. Cell* **27** 1898–910 Publisher: American Society for Cell Biology (MBOC)
- [103] Grosser S et al 2021 Cell and nucleus shape as an indicator of tissue fluidity in carcinoma *Phys. Rev. X* **11** 011033
- [104] Scott C et al 2017 Myosin II controls junction fluctuations to guide epithelial tissue ordering *Dev. Cell* **43** 480–92
- [105] Maitre J-L, Berthoumieux H, Krens S F G, Salbreux G, Julicher F, Paluch E and Heisenberg C-P 2012 Adhesion functions in cell sorting by mechanically coupling the cortices of adhering cells *Science* **338** 253–6
- [106] Foty R A and Steinberg M S 2005 The differential adhesion hypothesis: a direct evaluation *Dev. Biol.* **278** 255–63
- [107] Clapham D E 2007 Calcium signalling *Cell* **131** 1047–58
- [108] Chan C J, Ekpenyong A E, Golfier S, Li W, Chalut K J, Otto O, Elgeti J, Guck J and Lautenschläger F 2015 Myosin II activity softens cells in suspension *Biophys. J.* **108** 1856–69
- [109] Hosseini K, Frenzel A and Fischer-Friedrich E 2021 EMT changes actin cortex rheology in a cell–cycle-dependent manner *Biophys. J.* **120** 3516–3526
- [110] Jacob N et al 2016 Cellular contraction and polarization drive collective cellular motion *Biophys. J.* **110** 2729–38
- [111] Tom K et al 2019 The small GTPase Rac1 increases cell surface stiffness and enhances 3D migration into extracellular matrices *Sci. Rep.* **9** 7675
- [112] Tinevez J-Y, Perry N, Schindelin J, Hoopes G M, Reynolds G D, Laplantine E, Bednarek S Y, Shorte S L and Eliceiri K W 2017 TrackMate: an open and extensible platform for single-particle tracking methods *Image Process. Biol.* **115** 80–90
- [113] Zener C 1948 *Elasticity and Anelasticity of Metals* (Chicago, IL: University of Chicago Press)
- [114] Joseph D D 1990 *Fluid Dynamics of Viscoelastic Liquids* (New York: Springer)
- [115] Dong C and Chen B 2016 Temperature effect on the chemomechanical regulation of substeps within the power stroke of a single Myosin II *Sci. Rep.* **6** 19506
- [116] Kubitschke H, Morawetz E W, Käs J A and Schnauß J 2018 Physical properties of single cells and collective behavior *Quantification of Biophysical Parameters in Medical Imaging* ed I Sack and T Schaeffter (Berlin: Springer) pp 89–121
- [117] Warmt E, Kießling T R, Stange R, Fritsch A W, Zink M and Käs J A 2014 Thermal instability of cell nuclei *New J. Phys.* **16** 073009
- [118] Goettsch C, Kliemt S, Sinnigen K, von Bergen M, Hofbauer L C and Kalkhof S 2012 Quantitative proteomics reveals novel functions of osteoclast-associated receptor in STAT signaling and cell adhesion in human endothelial cells *J. Mol. Cellular Cardiol.* **53** 829–37
- [119] Schmidt J R, Vogel S, Moeller S, Kalkhof S, Schubert K, Bergen M and Hempel U 2019 Sulfated hyaluronic acid and dexamethasone possess a synergistic potential in the differentiation of osteoblasts from human bone marrow stromal cells *J. Cell. Biochem.* **120** 8706–22
- [120] Ong S-E, Blagoev B, Kratchmarova I, Kristensen D B, Steen H, Pandey A and Mann M 2002 Stable isotope labeling by amino acids in cell culture, SILAC, as a simple and accurate approach to expression proteomics *Mol. Cellular Proteomics* **1** 376–86
- [121] Mueller L N, Brusniak M-Y, Mani D R and Aebersold R 2008 An assessment of software solutions for the analysis of mass spectrometry based quantitative proteomics data *J. Proteome Res.* **7** 51–61
- [122] Hinkley D V 1969 On the ratio of two correlated normal random variables *Biometrika* **56** 635–9

- [123] Brody J P, Williams B A, Wold B J and Quake S R 2002 Significance and statistical errors in the analysis of DNA microarray data *Proc. Natl Acad. Sci.* **99** 12975–8
- [124] Hayya J, Armstrong D and Gressis N 1975 A note on the ratio of two normally distributed variables *Manage. Sci.* **21** 1338
- [125] Lei W *et al* 2016 Novel insights into the roles of Rho kinase in cancer *Arch. Immunol. Theor. Exp.* **64** 259–78